

# **Laser Sintering of Titanium Nanoparticles by Femtosecond Laser Irradiation with the Combined Molecular Dynamics and Two-Temperature Model**

An Undergraduate Thesis Submitted by

**Shahriar Karim Shafin (1810089)**

**Sudipta Debnath (1810106)**

**Farhan Kadir Rafi (1810069)**

Under the Supervision of

**Dr. Kazi Arafat Rahman**

Assistant Professor

Department of Mechanical Engineering

Bangladesh University of Engineering and Technology



A thesis submitted to the department of Mechanical Engineering, BUET  
in fulfillment of the requirements of the degree of Bachelor of Science  
in Mechanical Engineering

**Bangladesh University of Engineering and Technology**

**Dhaka-1000, Bangladesh**

**June-2024**

# Candidates' Declaration

This is to certify that the work presented in this thesis, titled, “Laser Sintering of Titanium Nanoparticles by Femtosecond Laser Irradiation with the combined molecular dynamics and two-temperature model”, is the outcome of the investigation and research carried out by us under the supervision of **Dr. Kazi Arafat Rahman**

It is also declared that neither this thesis nor any part of research work has been submitted anywhere else for the award of any degree, diploma or other qualifications.

---

Shahriar Karim Shafin  
1810089

---

Sudipta Debnath  
1810106

---

Farhan Kadir Rafi  
1810069

# Acknowledgement

We are profoundly grateful to our supervisor, **Dr. Kazi Arafat Rahman**, for his unwavering guidance, invaluable insights and steadfast support throughout the entire process of researching and writing this thesis. His expertise, patience, and constructive feedback have not only shaped the academic content of this work but also enhanced our growth. From outlining the initial research problem to making the outcome possible, his mentorship has been pivotal in every stage of this journey. We are truly fortunate to have had such a dedicated mentor who encouraged us to explore new perspectives and ideas.

We would also like to extend our heartfelt thanks to **Dr. Shahereen Chowdhury**, whose encouragement, expertise, and thoughtful advice were integral to the development and refinement of this thesis. Her mentorship and encouragement have been invaluable

We are also thankful to BUET for providing the necessary resources and environment conducive to research. This thesis wouldn't have been possible without the guidance and support of each, and everyone mentioned above.

# Contents

Candidates' Declaration	2
Acknowledgement	3
List of Symbols	6
List of Figures	7
List of Tables	8
1. Abstract	9
2. Introduction	10
3. Methodology and Simulation Details	14
3.1. Two-Temperature Model (TTM)	14
3.2. Molecular Dynamics:	15
3.3. Velocity-Verlet Algorithm	16
3.4. Combined TTM-MD	17
3.5. Simulation Details	20
3.5.1. Interatomic Potentials	21
3.5.2. Timestep	23
3.5.3. Energy Minimization	24
3.5.4. Statistical Ensembles	24
3.5.5. Simulation Software	25
3.6. Flow Chart of Sintering Process	29
4. Results and Discussion:	31
4.1. Temporal Evolutions of Electron and Lattice Temperature	31
4.2. Thermal Responses of electron and lattice subsystem	33

4.3. Visualizing the sintering process from atomistic snapshots	36
4.4. Insight into the structural transformation by common neighbor analysis	38
4.5. Amorphous Rate	41
4.6. Sintering parameters	42
4.6.1. Radial Distribution Function (RDF)	42
4.6.2. Mean Square Displacement (MSD)	44
4.6.3. Radius of Gyration	46
4.6.4. Shrinkage Ratio	48
4.6.5. Neck Radius	50
4.7. Effect of pulse width variation in sintering parameters	51
5. Conclusion	53
6. References	54

# List of Symbols

$T_e$	Electron temperature
$T_l$	Lattice temperature
$C_e$	Electron heat capacity
$C_l$	Lattice heat capacity
$K_e$	Electron thermal conductivity
$K_l$	Lattice thermal conductivity
$G$	Electron-phonon coupling factor
$S$	Laser power(W)
$F$	Laser fluence(J/m <sup>2</sup> )
$t_p$	Laser pulse width
$L_p$	Optical penetration depth
$k_b$	Boltzmann's constant
$\gamma_i$	Friction coefficient
$F_{0\Delta}$	Stability criterion
$\alpha$	Electron thermal diffusivity
$\rho_h$	Host electron density
$\phi_{ij}$	Pair-potential
$\epsilon$	Depth of the potential well
$\sigma$	Distance where potential is zero
$N$	Total no of atoms
$n$	Average no of atoms in a grid
$g$	Radial distribution function
$R_{gyr}$	Radius of gyration
$r_{com}$	Center of mass position
$\epsilon$	Shrinkage ratio
$l_0$	Distance between the centers of nanoparticles (t=0)
$l_t$	Distance between the centers of nanoparticles (t=t)

# List of Figures

<u>Figure-1.</u> Graphical Representation of Laser Sintering of two Ti NPs	29
<u>Figure-2.</u> Temporal evolutions of the electron temperature and lattice temperature of two Ti nanoparticles irradiated by a femtosecond laser with absorbed laser fluence $50 \text{ J/m}^2$ and pulse width 100 fs	31
<u>Figure-3.</u> Temporal evolutions of electron and lattice Temperature at (a) the constant pulse width of 100 fs but different fluence, F (b) the constant fluence of $50 \text{ J/m}^2$ but different pulse width, $t_p$	34
<u>Figure-4.</u> Atomistic Snapshots of Laser Sintering of Ti nanoparticles	37
<u>Figure-5.</u> Potential Energy Variation with Lattice Temperature at $50 \text{ J/m}^2$ fluence and 100 fs pulse width	39
<u>Figure-6.</u> Amorphous Rate with Time at constant pulse width of 100 fs for different laser fluences (i) $10 \text{ J/m}^2$ (Blue) (ii) $20 \text{ J/m}^2$ (Orange) (iii) $30 \text{ J/m}^2$ (Yellow) (iv) $40 \text{ J/m}^2$ (Purple) (v) $50 \text{ J/m}^2$ (Green)	40
<u>Figure-7.</u> RDF of Ti NPs at different temporal points at $50 \text{ J/m}^2$ fluence and 100 fs pulse width	42
<u>Figure-8.</u> Mean Square Displacement (MSD) variation with time at (a) constant pulse width 100 fs and (b) constant fluence $50 \text{ J/m}^2$	44
<u>Figure-9.</u> Radius of Gyration variation with time at (a) constant pulse width 100 fs and (b) constant fluence $50 \text{ J/m}^2$	46
<u>Figure-10.</u> Shrinkage Ratio variation with time at (a) constant pulse width 100 fs and (b) constant fluence $50 \text{ J/m}^2$	48

Figure-11. Neck Radius variation with time at (a) constant pulse width 100fs and (b) constant fluence 50 J/m<sup>2</sup> 49

## List of Tables

Table-1. Parameters used in the combined MD-TTM method on the sintering process 27

Table-2. Different combinations of absorbed laser fluence and laser pulse width on the sintering process 33



# 1. Abstract

In this study, the laser sintering process of titanium (Ti) nanoparticles through a simulation-based approach is explored. By employing a pair of Ti nanoparticles, each of which has a diameter of 6 nanometers, our objective is to gain an understanding of the various characteristics of the laser sintering process under varying fluence and pulse width conditions, as well as the melting temperature of the nanoparticles. In the literature, there are plenty of works where uniform linear heating was applied to simulate the sintering process of different nanoparticles. But laser heating is quite different from regular heating. To accurately model the laser heating mechanism, the two-temperature model (TTM) in conjunction with the molecular dynamics (MD) is used in this study which captures the rapid energy transfer between the electron and lattice subsystems that is typical of laser interactions. We analyze several key sintering parameters, including the radial distribution function (RDF), mean squared displacement (MSD), neck radius, shrinkage ratio and radius of gyration, to evaluate their variations in response to different laser fluences and pulse widths. Also, the atomistic snapshots are taken at different timesteps to better understand the sintering process and provide deeper insights into the laser sintering mechanisms of Ti nanoparticles.

## 2. Introduction

Additive manufacturing (AM) represents one of the pivotal trends in engineering and production, poised to exert a significant influence in the twenty-first century. Nanostructures, including nanoparticles and nanowires, have garnered considerable attention in additive manufacturing because of their distinctive properties and substantial potential in advancing a diverse array of applications. In recent times, the use of nano devices is getting increasingly popular, especially in the fields where high precision is necessary. Micro/nano additive manufacturing has been a hot topic over all the years which can produce devices with complex three-dimensional structures of different kinds of materials [1-3]. Titanium is one of the most popular materials having high corrosion and fatigue resistance, high tensile strength, high strength-to-weight ratio, lightweight, durable and whose alloys are used in producing high precision aerospace [4], medical equipment [5] and also recognized for their heavy utilizations in the automotive sector [6]. The reason for this widespread use is the superior properties of Titanium alloys compared to many other similar materials [7, 8]. For producing nano devices, conventional manufacturing processes do not yield good results and rapid prototyping technology can be used, which can produce devices with high dimensional accuracy and greater properties [9].

In selective laser melting processes, metallic nanoparticles can be used as raw material to produce high quality products at low cost and with increased functionality [10, 11]. Laser sintering using a femtosecond laser can provide high precision and accuracy where the particles don't completely melt but change their form and structure under the melting point [12, 13]. So, for materials having high melting point, laser sintering is a good option compared to laser melting. In the previous study, sintering with constant heat flux had been performed for different kinds of materials [14, 15]. Selective laser sintering is one of the rapid prototyping methods, more practical scenario which can process metals, polymers and various types of composites [16].

Powder bed additive manufacturing stands as a state-of-the-art method in contemporary manufacturing where complex components are built layer by layer from powder materials by partial or complete melting facilitated by either electrons or a laser beam. The use of femtosecond lasers for additive manufacturing has a specific experimental foundation, which is mostly used for Two-photon polymerization [17, 18], Projection Micro Stereolithography (PμSL) [19, 20], Continuous Liquid Interface Production (CLIP) [21], Electrohydrodynamic (EHD) Jet Printing [22, 23], Aerosol Jet (AJ) Deposition, and Micro-Selective Laser Melting (Micro-SLM) [24]. MNAM has successfully produced various Micro/Nano Functional Devices (MNFDs) like micro-actuators [25, 26], micro batteries / supercapacitor [27, 28], micro/nano-optics [29], and multi-scale bioactive scaffolds [30].

In nanoparticle sintering, a lot of numerical and experimental work has been done to examine the femtosecond laser interaction with metallic nanoparticles. Yang *et al.* identifies that the final formation of the sintered particle is irrelevant to the heating rate when the sintering process continues long enough to turn the solid particle pairs into a liquid state for different heating rates [31]. Zhang *et al.* showed that higher heating rate during sintering increases the mechanical strength of the sintered material [32]. Transient heat conduction is used to measure the temperature and at that temperature MD simulation reveals the microstructure, high laser power ensures better sintering performance [33]. Laser parameters as well as sintering parameters are investigated by Huang *et al.* for Cu nanoparticles with the modified MD-TTM model [34]. Nandy *et al.* established uneven sized particles go for greater coalescence than evenly sized particles, diffusion rate is faster in unequal sized particles for different kind of alloys [35-37]

Titanium and its alloys have piqued the interest of scientists for many years in the sintering process. Rahmani *et al.* performed molecular dynamics (MD) simulation to gain important molecular insights regarding melting as well as the solidification behavior of two economically significant core/shell alloys for pure Ti, Cu, Al and their alloys [38]. Jeon *et al.*

performed mechanical properties of sintered Ti “NP-chains” and the thermal parameters of the sintering process for different heating rate and temperature due to the femtosecond laser irradiation [39]. Lai *et al.* showed the physical parameters of nanoscale Ti-Al alloy power during laser sintering process under different constant heating rates [40]. Koparde *et al.* determined the melting point of TiO<sub>2</sub> nanoparticles by the sintering process using molecular dynamics and phenomenological modeling for different sizes [41]. Dal Forno *et al.* showed the electron-phonon coupling and electron thermalization behavior in titanium nitride nanoparticles [42]. Microstructures and mechanical properties of commercially pure porous titanium had been analyzed in the previous study by the sintering phenomenon [43, 44]

However, the preceding researches were restricted to predicting the melting temperature and structural evolution of nanoparticles on an atomic scale. When simulating the sintering phenomenon, the earlier works used a fixed heating rate without replicating the physical scenario of femtosecond laser contact with nanoparticles [45-47]. The previous studies didn't consider the electron excitation and non-equilibrium phenomena between electron and lattice due to the femtosecond laser irradiation during the sintering process [48]. When a femtosecond laser is applied on metallic materials, the electron subsystem absorbs laser energy and electron excitation occurs consequently. The absorbed laser energy is then transferred from the electron subsystem to the lattice subsystem (two temperature model) [49]. So, when developing a sintering model for researching femtosecond laser interactions with nanoparticles, the electron subsystem must be considered [50]. For this reason, the combined MD-TTM model has been introduced in our sintering process for titanium.

Many researches regarding TTM has been performed and improved due to ultrashort laser pulses in the past decades [51-54]. But the previous works expanded the combined MD-TTM model for the laser melting and laser ablation process due to laser pulse heating in the pico-femtosecond range. Ivanov *et al.* performed the combined atomistic-continuum modeling for short-pulse laser melting and laser ablation process of Ni and Au, observed the thermal

conductivity and electron-lattice non-equilibrium phenomena of metals [55]. Zhang *et al.* examined the melting temperature and solidification behavior of Au nanoparticles due to ultrashort laser pulses [56]. Ultrafast laser sintering of metallic nanoparticles considering the electron-lattice non-equilibrium condition didn't go to that extent which is a physical scenario in most of the cases. Besides, they ignored the electron excitation and characteristics during the sintering process as mentioned above. To the best of our knowledge, Guo *et al.* observed the femtosecond laser sintering behavior of Al nanoparticles with the combined MD-TTM model and represented the sintering parameters as well [57].

In the present study, our main objective is to conduct a multiscale investigation of the combined MD-TTM model for the Titanium nanoparticles under the femtosecond laser irradiation process. In this context, we aim to investigate the spatiotemporal details of titanium nanoparticles and impacts of femtosecond laser parameters on the sintering process. Furthermore, the temporal changes of electron temperature, lattice temperature, atomistic snapshots in addition to the performance and sintering parameters such as radial distribution function, radius of gyration, mean square displacement, radius ratio, shrinkage rate, common neighbor analysis under different fluences and pulse widths will be extensively explored for titanium nanoparticles.

## 3. Methodology and Simulation Details

### 3.1. Two-Temperature Model (TTM):

In our current study, we utilized a two-temperature model to monitor the energy transfer between the electron and lattice subsystems during femtosecond laser irradiation. The two-temperature model explains the energy changes in the electron and lattice subsystems over a brief period, often in the femtosecond or picosecond timescale. When an ultrafast laser is directed at a system, the electron subsystem excites rapidly, and the electron subsystem mostly absorbs the laser energy. This creates a temporary state of imbalance between the electron and lattice subsystems. Subsequently, the lattice subsystem absorbed energy from the electron through electron-phonon coupling. An energy exchange occurs between the electron and lattice subsystems due to electron-phonon coupling processes [58].

The entire system's behavior can be represented by the following partial differential heat diffusion equations (PDEs) [50, 51] for metallic nanoparticles.

$$C_e \frac{\partial T_e}{\partial t} = \nabla[K_e \nabla T_e] - G(T_e - T_l) + S(z, t) \quad (i)$$

$$C_l \frac{\partial T_l}{\partial t} = \nabla[K_l \nabla T_l] + G(T_e - T_l) \quad (ii)$$

Here,  $C_e$  and  $C_l$  represent the heat capacity of the electron and lattice subsystems, respectively, whereas  $K_e$  and  $K_l$  represent the thermal conductivity of the electron and lattice subsystems. The energy transmission between the electronic and lattice subsystems in the heat diffusion equations is denoted by the second term on the right side of the equations. The coupling factor,  $G$ , determines the energy exchange influenced by the temperature differential between the electronic and lattice subsystems.  $S(z, t)$  signifies the Gaussian laser profile, whereas  $G$  symbolizes the electron-phonon coupling phenomenon.  $T_e$  and  $T_l$  represent the temperatures of the electron and lattice subsystems, respectively.

The source term represents the Gaussian profile [53, 59] as follows:

$$S(z, t) = \sqrt{\frac{4 \ln(2)}{\pi}} \frac{F}{t_p L_p} \exp \left[ -\frac{z}{L_p} - 4 \ln(2) \left( \frac{t - 2t_p}{t_p} \right)^2 \right] \quad (\text{iii})$$

Here,  $F$  is the laser fluence,  $t_p$  is the pulse width (full-width half maximum), and  $L_p$  is the optical penetration depth.

### 3.2. Molecular Dynamics:

Molecular dynamics (MD) is a powerful computational simulation technique used to study the physical movements and interactions of atoms and molecules over time. By modeling the dynamic evolution of molecular systems, MD provides detailed insights into the microscopic behaviors that underpin a wide range of physical, chemical, and biological processes.

At its core, MD simulates the behavior of a system of particles by solving Newton's equations of motion. Each particle, representing an atom or molecule, is assigned initial positions and velocities. The interactions between particles are described using mathematical functions known as force fields, which account for both bonded interactions (such as covalent bonds, angles, and dihedral angles) and non-bonded interactions (such as van der Waals forces and electrostatic forces) and after that it updates each atoms' position, velocities and forces between them in every timestep with the help of velocity-Verlet algorithm [60].

Starting from an initial configuration, often derived from experimental data such as X-ray crystallography or NMR spectroscopy, the MD simulation calculates the forces acting on each particle, updates their positions and velocities through small, discrete time steps (typically on the order of femtoseconds), and often employs periodic boundary conditions to mimic an infinite system and eliminate edge effects. This approach allows for the detailed exploration of various phenomena, including the folding and dynamics of proteins, the properties of materials at the atomic scale, the pathways of chemical reactions, and the interactions between drug molecules and their biological targets. Despite being computationally intensive, advancements

in algorithms, high-performance computing (e.g., GPU utilization), and enhanced sampling techniques are continuously pushing the boundaries of MD, making it an invaluable tool in fields such as biophysics, materials science, chemistry, and pharmaceutical research.

### **Classical Newton's equation of motion:**

Newton's second law states the relationship between the mass and acceleration of a particle to the force acting on that particle [61].

$$F_i = m_i a_i = m_i \frac{d^2 r_i}{dt^2} \quad (\text{iv})$$

From the classical mechanics, this equation can be written as the function of potential energy of the particle at position  $r_i$ .

$$m_i \frac{d^2 r_i}{dt^2} = - \frac{dU(r_i)}{dr_i} \quad (\text{v})$$

### **3.3. Velocity-Verlet Algorithm:**

The velocity-Verlet algorithm is a widely used integration method in molecular dynamics simulations for updating the positions, velocities, and accelerations of particles over discrete time steps. It is favored for its simplicity, stability, and time-reversibility.

Velocity- Verlet algorithm is frequently implemented algorithm to obtain positions, velocities and accelerations at time  $t + \delta t$  from the respective quantities at time  $t$ .

At the beginning of each time step, we have the positions  $r_i(t)$ , velocities  $v_i(t)$ , and accelerations  $a_i(t)$  of all particles  $i$ .

For each integration cycle, it updates the velocities at the half time step:

$$v_i \left( t + \frac{\Delta t}{2} \right) = v_i(t) + \frac{1}{2} a_i(t) \Delta t \quad (\text{vi})$$

After that, it updates the positions using the half-step velocities:

$$r_i(t + \Delta t) = r_i(t) + v_i \left( t + \frac{\Delta t}{2} \right) \Delta t \quad (\text{vii})$$



Then, the algorithm calculates the new forces  $F_i(t + \Delta t)$  based on the updated positions  $r_i(t + \Delta t)$  and update the accelerations  $a_i(t + \Delta t) = \frac{F_i(t + \Delta t)}{m_i}$  where  $m_i$  is the mass of particles  $i$ .

Therefore, it updates the velocities for the new time step and the process further goes on repeatedly for next time steps.

$$v_i(t + \Delta t) = v_i\left(t + \frac{\Delta t}{2}\right) + \frac{1}{2}a_i(t + \Delta t)\Delta t \quad (\text{viii})$$

This algorithm can be implemented without much complexity and works well for both short and long timesteps [62]. By following the steps above, the velocity-Verlet algorithm allows molecular dynamics simulations to track the trajectories of particles accurately, providing valuable insights into the dynamic behavior of molecular systems.

### 3.4. Combined TTM-MD:

The two-temperature model, a novel approach, effectively describes the energy development of electron and lattice subsystems but does not account for atomic-scale phenomena such as sintering kinetics, defect creation, and melting. The integration of molecular dynamics simulation, a well-established method, can be quite informative in this context. Traditional molecular dynamics relies on classical Newtonian mechanics [63] and calculates an atoms' motion using the velocity-Verlet algorithm [64]. Integrating the electron subsystem into the modelling process is challenging; however, it is essential for the initial energy excitation caused by ultrafast laser irradiation.

Modelling the electronic subsystem as a system of classical particles is challenging in MD simulations due to the electron's lower mass and faster reaction time than atoms.

A semi-classical TTM-MD approach is utilized to simulate the impact of ultrafast laser irradiation on an atomic timescale.

The combined TTM-MD model replaces the parabolic partial differential equation of the lattice subsystem(ii) with the classical Newtonian equation of molecular dynamics [65].

$$\frac{md^2r_i}{dt^2} = F_i - \gamma_i v_i + p \sqrt{\frac{k_b T_e \gamma_i m}{\Delta t}} \quad (\text{ix})$$

Here,  $m$  and  $r_i$  represent the mass and displacement of an atom. The force experienced by a particular atom due to interatomic contact is denoted as  $F_i$ .  $\gamma_i v_i$  defines the friction term that models the energy dissipation of an atom caused by electron-phonon interaction. The increase in atoms' energy due to the interaction with electrons is represented by a stochastic force term with a random magnitude and direction.

The electron subsystem temperature ( $T_e$ ) and the friction coefficient ( $\gamma_i$ ) determine the amount of the stochastic force.  $k_b$  is the Boltzmanns' constant whereas  $\Delta t$  is time needed to get into collision. The vector,  $p$  has a random magnitude and direction. The TTM-MD model is solved by dividing the simulation cell into a finite number of grid cells, each housing several atoms.

The connection between the electronic heat diffusion equation and the Molecular dynamics equation is established through the energy balance in individual grid cells.

In a particular grid cell, the energy loss of an  $i^{th}$  atom  $\Delta U_i$  due to the friction force  $\gamma_i v_i$  at MD time step  $\Delta t$  is given by,

$$\Delta U_i = \gamma_i v_i^2 \Delta t \quad (\text{x})$$

Now, total energy loss in a particular grid cell containing  $N$  number of atoms is given by,

$$\Delta U_l = \Delta t \sum_{i=1}^N \gamma_i v_i^2 \quad (\text{xi})$$

Now, energy gain of the electron subsystem in each time step is,

$$\Delta U_e = G T_l \Delta V \Delta t \quad (\text{xii})$$

Where,  $\Delta V$  is the volume of the grid cell.

Now we define temperature and energy relation in a grid cell,

$$\frac{3}{2}k_b T_l = \frac{1}{N} \sum_{i=1}^N \frac{1}{2} m v_i^2 \quad (\text{xiii})$$

Now, the energy loss of the lattice subsystem must be equal to the energy gain of the electronicsubsystem. So, from equation (xi) and (xii) we find,

$$\sum_{i=1}^N \gamma_i v_i^2 = G T_l \Delta V \quad (\text{xiv})$$

Now combining equations (xiii) and (xiv), we find,

$$\gamma_i = \frac{G \Delta V m}{3 N k_b} \quad (\text{xv})$$

The material constants for the electronic subsystem were obtained from Lin *et al* (2008) [66].

The heat capacity,  $C_e$  of the electronic subsystem is represented by,

$$C_e = \gamma T_e \quad (\text{xvi})$$

where  $\gamma = 328.9 \text{ Jm}^{-3}\text{K}^{-2}$ .

The thermal conductivity,  $K_e$  of the electronic subsystem is defined [55] by,

$$K_e = K_o * (T_e/T_l) \quad (\text{xvii})$$

where  $K_o = 21.9 \text{ Wm}^{-1}\text{K}^{-1}$ .

The electron temperature-dependent coupling factor, denoted as  $G$ , is determined from Lin *et al* (2008) for titanium nanoparticles. Additionally, the optical penetration depth for titanium, represented as  $L_p$ , is found to be 15.2 nm [67].

The electron temperature is now determined using the finite difference technique (FDM). The stability criterion,  $F_{0\Delta}$  for the finite difference scheme is dictated by the length of each grid cell along the X, Y, and Z axis, denoted as  $\Delta x$ ,  $\Delta y$ , and  $\Delta z$  [55]. \

$$F_{0\Delta} = \frac{\alpha \Delta t}{\Delta x^2 + \Delta y^2 + \Delta z^2} \leq 0.5 \quad (\text{xviii})$$

Where the thermal diffusivity,  $\alpha = \frac{K_e}{C_e}$  (xix)

### 3.5. Simulation Details:

A box with dimensions of 120 Å\*180 Å\*120 Å is formed for the molecular dynamics simulation. The electrical temperature computation involves dividing the simulation cell into 20\*30\*20 cells along the X, Y and Z axes.

The bulk structure of pure Ti nanoparticles is HCP (Hexagonal Close-Packed). But the structure of Ti NPs greatly depends on its size and temperature. However, a size-dependent HCP-to-FCC transition is observed at temperatures below 600K and around a Ti NP diameter of 6nm [68] Initially, the simulation cell is occupied with titanium atoms arranged in a face-centered cubic (FCC) arrangement ((lattice constant: 0.434 nm). Next, two spherical regions with a diameter of 6nm each are identified and marked. The atoms outside the specified region have been removed, forming a two-contacted Ti nanoparticle system. The entire process of creating the Ti nanoparticles' structure is carried out using the ATOMSK software. After that, the system is maintained at 298 K for 2 ns using the Noose-Hoover thermostat to achieve a state of relaxation and the NVT canonical ensemble is conducted to maintain the constant temperature.

Following relaxation, the system underwent ultrafast single pulse laser irradiation with varying fluence and pulse width. We monitored the temperature changes in the electronic and lattice subsystems during laser irradiation and observed the sintering kinetics. The classical embedded atom method (EAM) has been widely adopted to study interactions of metallic nanoparticles [69]. The EAM potential is utilized for interatomic interaction, using parameterization derived from Zhou *et al* (2004) [70]. In the embedded-atom method, the total energy of a system is represented as-

$$E_{total} = \sum_i F_i(\rho_{h,i}) + \frac{1}{2} \sum_i \sum_{j(\neq i)} \phi_{ij}(r_{ij}) \quad (xx)$$

Here,  $\rho_{h,i}$  is the host electron density at atom  $i$  due to the remaining atoms of the system,  $F_i(\rho_{h,i})$  is the energy to embed atom  $i$  into the back-ground electron density  $\rho$ , and  $\phi_{ij}(r_{ij})$  is a pair potential as a function of distance  $r_{ij}$  between atoms  $i$  and  $j$ .

The entire TTM-MD system, meticulously developed with the LAMMPS (Large-scale Atomic/Molecular Massively Parallel Simulator) simulation program, ensures the highest level of precision in our research [71]. OVITO software, a powerful visualization tool, is utilized to provide clear and comprehensive visual representations of our simulations [72].

### 3.5.1. Interatomic Potentials:

Interatomic potentials, also known as force fields, are mathematical models used to describe the interactions between atoms and molecules in a system. These potentials are essential for molecular dynamics simulations as they define the forces that govern the motion of atoms. Interatomic potentials can be categorized into various types based on the nature of the interactions they model, ranging from simple pairwise potentials to more complex many-body potentials.

The potential energy of the system is expressed as a function of the positions of the nuclei when they are arranged in a specific configuration. The relative positions of the atoms with relation to one other are commonly utilized to define it, rather than their absolute positions. The general structure in the one following:

$$U(r_1, r_2, r_3, \dots) = V_1 + V_2 + V_3 \quad (\text{xxi})$$

Here,  $V_1, V_2, V_3$  represent different contributions to the total potential energy.  $V_1$  refers to the single body potential which typically represents the potential energy associated with external fields or intrinsic properties of individual atoms. In many practical interatomic potentials, this term is often absent unless an external field or specific boundary conditions are considered.

$$V_1 = \sum_i U_{\text{external}}(r_i) \quad (\text{xxii})$$

$V_2$  refers to the two-body potential which describes the interactions between pairs of atoms. This is the most common type of interaction and includes van der Waals forces, Coulombic interactions, and bonded interactions. For example, the Lennard-Jones potential and the Coulomb potential are two-body potentials.

$$V_2 = \sum_{i < j} V_{ij}(r_i, r_j) \quad (\text{xxiii})$$

Where  $V_{ij}$  is a function describing the interaction between atom  $i$  and atom  $j$ . For the Lennard-Jones potential, this would be:

$$V_{ij}(r_i, r_j) = 4\epsilon \left[ \left( \frac{\sigma}{r_{ij}} \right)^{12} - \left( \frac{\sigma}{r_{ij}} \right)^6 \right] \quad (\text{xxiv})$$

Where  $r_{ij} = |r_i - r_j|$  is the distance between atoms  $i$  and  $j$ ,  $\epsilon$  is the depth of the potential well, and  $\sigma$  is the distance at which the potential is zero.

$V_3$  refers to the three-body potential which considers the interactions among triplets of atoms. These potentials are crucial for accurate modeling systems with directional bonding, such as covalent bonds in silicon or carbon structures. Three-body potentials can capture the dependence of the potential energy on bond angles.

$$V_3 = \sum_{i < j < k} V_{ijk}(r_i, r_j, r_k) \quad (\text{xxv})$$

An example of a three-body potential is the Stillinger-Weber potential used for silicon, which includes terms that depend on both bond lengths and bond angles:

$$V_{ijk}(r_i, r_j, r_k) = \lambda (\cos \theta_{ijk} - \cos \theta_0)^2 \quad (\text{xxvi})$$

where  $\theta_{ijk}$  is the angle between the bonds  $r_{ij}$  and  $r_{ik}$ , and  $\lambda$  and  $\theta$  are parameters specific to the material.

While  $V_1, V_2, V_3$  are the most used terms, higher-order potentials can also be included for more accurate descriptions of complex systems. These involve interactions among four or more atoms simultaneously. However, such terms are computationally expensive and less commonly used unless the system's nature strongly necessitates them [73, 74].

Some potentials incorporate the effects of interactions between multiple particles, including three or more, in their calculation of potential energy. Some simulations utilizing two-body potentials have incorporated multi-body dependencies to accurately replicate the interactions between multiple bodies.

However, in the context of many-body potentials, these interactions are computed by combining higher-order variables. Constant parameter averaging is necessary for the interatomic potential due to its approximations to some reference values. Simple potentials such as the Leonard-Jones potential can be readily adjusted to, for instance, correspond to the cohesive energy of a solid or the equilibrium bond length and binding strength of a dimer molecule. In contrast, many-body potentials can possess numerous adjustable parameters, ranging from dozens to even hundreds. This factor should be included when examining a larger set of experimental data or when studying the properties of materials predicted by simpler simulation models, such as density functional theory.

### **3.5.2. Timestep:**

When it comes to MD simulation, the time step is one of the most essential elements since it has the potential to influence both the amount of processing that is required and the amount of time that the simulation takes. When it comes to choosing a time step, there are two characteristics that must be satisfied. The first important consideration is that the time step must be sufficiently tiny to ensure that the simulation is accurate and that the motion of the atoms is continuous. The second requirement is that the time step must be sufficiently large to avoid running the simulation for an unduly long period of time. There are times when it is possible to choose a time step that is not constant, which will result in an increase in the efficiency of the simulations. It comes in handy when performing simulations on a big scale or when the velocities of the atoms fluctuate while the simulation is being run. Lastly, but certainly not

least, it is important to emphasize that a simulation can be regarded as "valid" when the running duration of the simulation is longer than the relaxation times of the essential properties.

### **3.5.3. Energy Minimization:**

During a molecular dynamics simulation, energy minimization is performed to determine the lowest potential energy of the system. Gradient optimization is frequently employed to achieve energy minimization. The objective of energy minimization is to identify the most efficient route or path from a starting configuration to the subsequent configuration with the lowest energy.

### **3.5.4. Statistical Ensembles:**

A Molecular Dynamics (MD) simulation can be conducted under several settings, commonly known as ensembles, which is a technical word used in statistical mechanics. A thermodynamic ensemble allows for the determination of the thermodynamic characteristics of a system by utilizing the principles of classical and quantum mechanics. The mathematical techniques required to comprehend the derivation of thermodynamic quantities will not be extensively elaborated upon. The core concept is that various ensembles embody systems with varying levels of detachment from the surrounding world, spanning from entirely isolated systems (microcanonical ensemble) to entirely open ones (grand canonical ensemble). The selection of the ensemble is contingent upon the challenge at hand and the desired conditions for simulating the system [\[75\]](#).

In the microcanonical NVE ensemble, the system has constant moles (N), volume (V), and energy (E). The microcanonical ensemble, therefore, corresponds to an isolated system that cannot exchange heat or matter with the outer environment.



The canonical NVT ensemble maintains constant values for the number of moles (N), volume (V), and temperature (T). In this scenario, the system is permitted to transfer heat to the surrounding outside space to maintain a constant temperature. One way to conceptualize it is as a system that is fully submerged within a colossal thermostat.

In the isothermal-isobaric NPT ensemble, pressure (P), temperature (T), and moles (N) are conserved. This ensemble is more adaptable than the one we previously observed. The system is permitted to exchange heat while simultaneously regulating the volume to maintain a consistent pressure where the volume (V), temperature (T), and chemical potential (M) remain constant in the grand-canonical MVT ensemble.

### **3.5.5. Simulation Software:**

#### **LAMMPS:**

LAMMPS (Large-scale Atomic/Molecular Massively Parallel Simulator) is a versatile and powerful software tool developed by Sandia National Laboratories, specifically designed for performing molecular dynamics simulations across a wide range of scientific disciplines. One of its standout features is its ability to efficiently harness the computational power of parallel computing architectures using MPI (Message Passing Interface). This allows LAMMPS to distribute computational tasks among multiple processors, making it scalable for simulating large systems containing millions to billions of atoms.

The software supports an extensive library of interatomic potentials, encompassing pairwise potentials such as Lennard-Jones and Coulomb interactions, many-body potentials like the Embedded Atom Method (EAM) and Tersoff potentials, and bonded potentials for modeling covalent bonds and angle bending. This flexibility makes LAMMPS suitable for simulating diverse materials ranging from metals and semiconductors to polymers, biomolecules, and colloids. It also offers various boundary conditions, including periodic and non-periodic setups,

and integrates advanced algorithms for temperature and pressure control, essential for accurately representing real-world thermodynamic conditions in simulations. Researchers and engineers rely on LAMMPS for its customizable script-based input format, allowing precise control over simulation parameters and easy adaptation to specific research needs. Output from LAMMPS provides detailed information on system properties such as energies, forces, and trajectories, facilitating in-depth analysis of molecular dynamics phenomena and supporting discoveries in fields such as materials science, chemistry, biophysics, and nanotechnology.

### **ATOMSK:**

Atomsk is a versatile command-line tool and library designed for creating, manipulating, and converting atomic configurations used in atomistic simulations and materials science. Developed by Pierre Hirel, Atomsk offers a range of functionalities essential for preparing atomic structures for simulations. It can generate initial configurations for various crystal structures, including cubic and hexagonal lattices, with options to specify lattice constants and supercell dimensions.

Atomsk supports seamless conversion between popular file formats such as XYZ, POSCAR/CONTCAR, CIF, and LAMMPS data format, enabling compatibility across different simulation software. Its capabilities extend to manipulating atomic positions, adding or removing atoms, and applying deformations or generating defects like vacancies and dislocations [76]. This flexibility is crucial for studying material properties under different conditions. Atomsk operates efficiently through a command-line interface, facilitating batch processing and automation of complex simulation setups. It is widely utilized in research for its reliability, ease of integration into existing workflows, and its ability to streamline the preparation of input files for molecular dynamics simulations and electronic structure calculations.

**OVITO:**

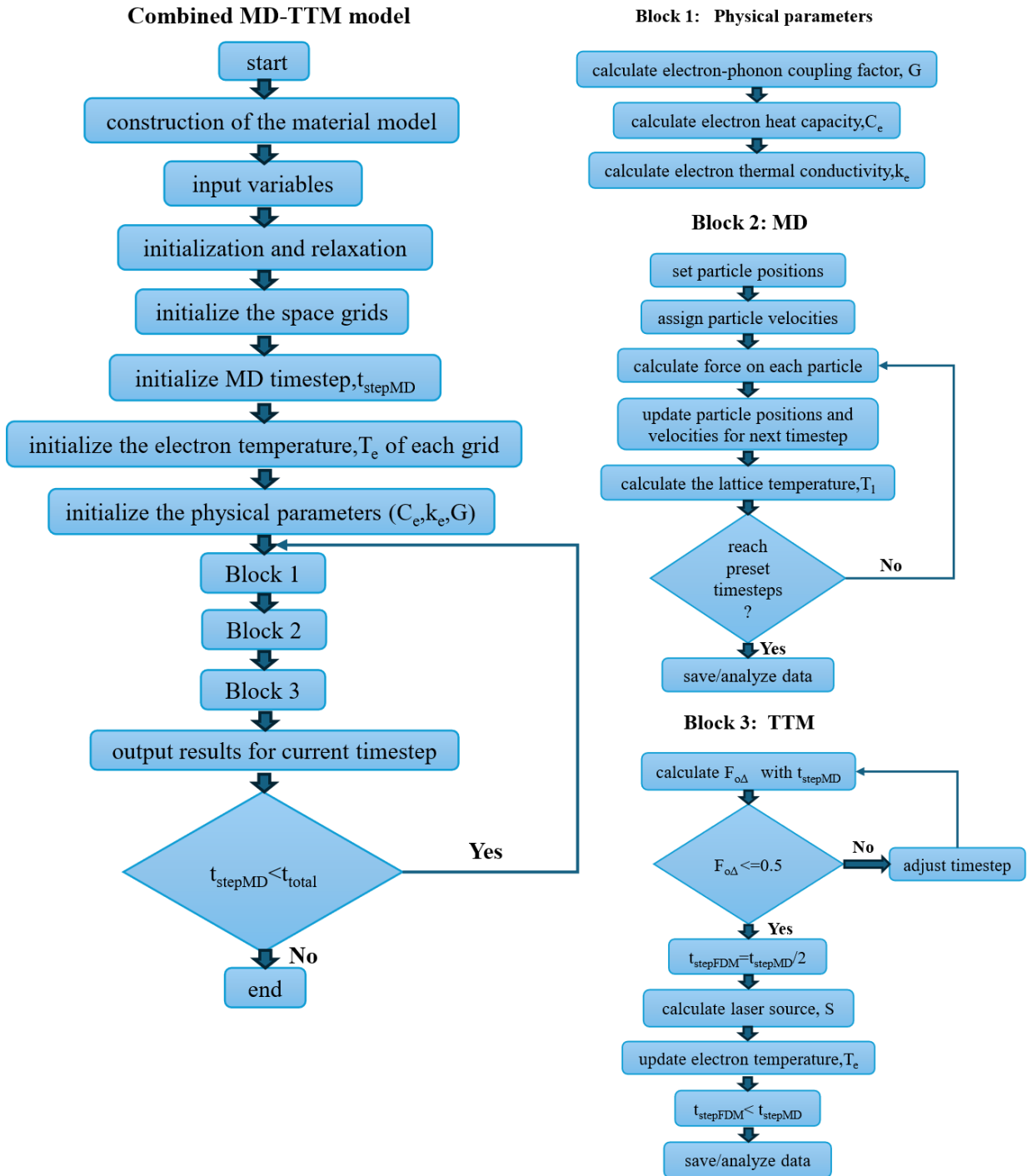
OVITO, an acronym for Open Visualization Tool, is a software program that creates a meaningful graphical representation from a system's raw atomic coordinates, which are generated by LAMMPS. The display and interpretation of atomistic datasets generated by Monte-Carlo simulation and large-scale molecular dynamics are made possible by the free and open-source software OVITO. OVITO's visualization capabilities include rendering atomic structures in 3D, visualizing particle trajectories, and generating insightful graphical representations of simulation data, such as radial distribution functions and Voronoi tessellations.

Moreover, it offers comprehensive analysis tools for quantifying properties like coordination numbers, defects, and grain boundaries in materials. OVITO's user-friendly interface and scripting capabilities make it accessible for both novice users and advanced researchers, providing valuable insights into the structural and dynamical behavior of complex systems simulated at the atomic scale.

**Table 1:** Parameters used in the combined MD-TTM method in the sintering process

Physical parameter	Symbol	Value		Unit
Electron heat capacity	$C_e$	$\gamma \cdot T_e$	$\gamma = 328.9 \text{ Jm}^{-3}\text{K}^{-2}$	$\text{Jm}^{-3}\text{K}^{-1}$
Electron thermal conductivity	$K_e$	$K_0 \cdot (T_e/T_1)$	$K_0 = 21.9 \text{ Wm}^{-1}\text{K}^{-1}$	$\text{Wm}^{-1}\text{K}^{-1}$
Optical penetration depth	$L_p$	15.2		nm
Electron-phonon coupling factor	$G$	$(A_1 \cdot \exp(-((T_e - B_1)/C_1)^2) + A_2 \cdot \exp(-((T_e - B_2)/C_2)^2) + A_3 \cdot \exp(-((T_e - B_3)/C_3)^2))$		$\text{Wm}^{-3}\text{K}^{-1}$
Constant	$A_1$	3.796e+18		K
Constant	$B_1$	5221		K
Constant	$C_1$	3337		K
Constant	$A_2$	1.297e+18		K
Constant	$B_2$	1955		K
Constant	$C_2$	2037		K
Constant	$A_3$	2.99e+17		K
Constant	$B_3$	740.7		K
Constant	$C_3$	719.2		K
Cell/grid size	$\Delta x, \Delta y, \Delta z$	6		nm
Timestep	$\Delta t$	1		fs

### 3.6. Flow Chart of Sintering Process:



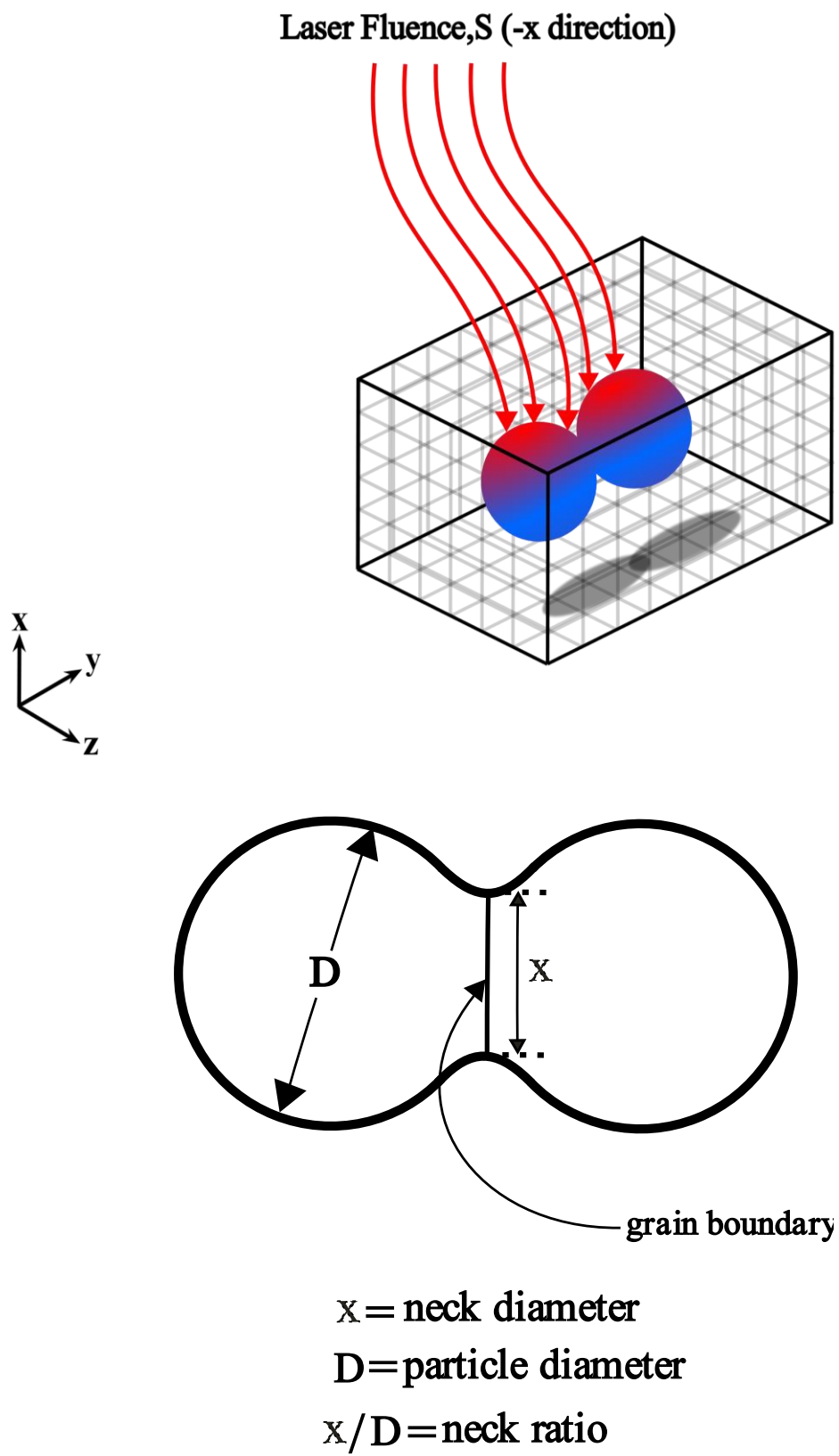


Figure-1: Graphical Representation of Laser Sintering of two Ti NPs

## 4. Results and Discussion:

### 4.1. Temporal Evolutions of Electron and Lattice Temperature:

The temporal evolutions of electron temperature ( $T_e$ ) and lattice temperature ( $T_l$ ) during the femtosecond laser sintering of Ti nanoparticles are monitored, as depicted in Figure-2. The figure above gives us a crystal-clear idea about how the electron and lattice temperature changes during the sintering process due to the ultrashort laser heating in the picosecond timescale. Mention that it's a single-pulse laser where the pulse width,  $t_p$  of the laser, is in the femtosecond range. In the figure, the dashed line corresponds to the electron temperature,  $T_e$ , whereas the solid line indicates the lattice temperature,  $T_l$ . The temporal changes of electron and lattice temperatures can be divided into three stages, as illustrated in the figure by two vertical black dashed lines. The first stage is where the femtosecond laser excites the electron subsystem, and as a result, the temperature of the electrons experiences a rapid, non-linear increase with time. It is non-linear because as the electron temperature increases, the electron heat capacity ( $C_e$ ) also increases. Electron heat capacity,  $C_e$ , is proportional to electron temperature,  $T_e$ , as described earlier. At the end of the first stage, the electron temperature peaks at 2942K at 0.3 ps. On the other hand, the lattice temperature doesn't increase that much in this short period, undergoing a minor rise to 548K. The temperature gap between  $T_e$  and  $T_l$  becomes more noticeable as time progresses. The coupled energy transport between electrons and phonons has a slightly adverse impact on electron heating. At the same time, it speeds up lattice heating, and it can be verified from the TTM (two-temperature model) equations mentioned earlier.

The prominent temperature increase in the lattice subsystem undergoes in the second stage from 0.3 ps to 12 ps, where electron temperature starts to decrease rapidly from the initial point (0.3 ps), and the deposited laser energy transfers to the cold lattice subsystem. As a result,

the temperature of the lattice rises gradually until both the electron and lattice subsystem reach an equilibrium point at 12 ps. The thermal equilibrium temperature at the end of stage two is 1423K during the sintering process under the femtosecond laser of 50 J/m<sup>2</sup> fluence and 100 fs pulse-width, which is the maximum lattice temperature.

The third stage begins at 12 ps, during which the electron and lattice temperatures remain in thermal equilibrium throughout the stage. After that, neither the electron nor the lattice temperatures exhibit any further increase or decrease. The temperature vs. time profile mirrors the findings from the TTM documented in other studies [16, 57, 77]. In the MD simulation, the canonical NVE ensemble was implemented after the laser excites the electron subsystem at first from 0 ps. For that, there is no chance of exchanging energy from outside to the lattice or electron subsystem during simulation, and both electron and lattice temperatures equilibrate around 1423K at the end of the simulation at 100 ps.

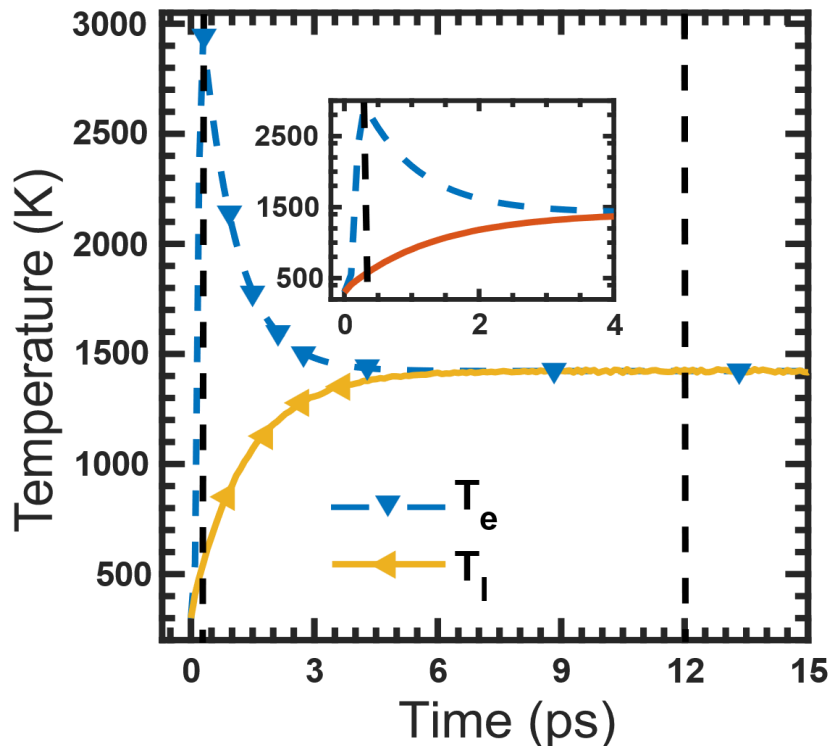


**Figure-2: Temporal evolutions of the electron temperature and lattice temperature of two Ti nanoparticles irradiated by a femtosecond laser with absorbed laser fluence 50 J/m<sup>2</sup> and pulse width 100 fs.**



## 4.2. Thermal Responses of electron and lattice subsystem

In Fig.3(a), it can be seen that laser pulse width,  $t_p$ , is fixed at 100 fs and laser fluences,  $F$ , vary with an interval of 10 J/m<sup>2</sup>. Electron temperature,  $T_e$ , reaches its peak value within the sub-picosecond time frame. Besides, it is observed that the higher the laser fluence, the higher the peak temperature,  $T_e$ . It is important to note that the increase of the peak electron temperature with laser fluence doesn't follow a linear pattern in the figure. The rate of this increment of peak temperature decreases as laser fluence increases.

When  $F$  is raised from 10 J/m<sup>2</sup> to 20 J/m<sup>2</sup>, peak temperature,  $T_e$  increases by about 525K, whereas peak temperature only increments around 300K from 40 J/m<sup>2</sup> to 50 J/m<sup>2</sup>. This is because electron heat capacity  $C_e$  is proportional to electron temperature,  $T_e$  [53]. When it comes to lattice temperature,  $T_l$ , it is noticeable that the increment rate of lattice temperature decreases from 10 J/m<sup>2</sup> to 50 J/m<sup>2</sup>, as well as the equilibrium gap. When laser fluence,  $F$  increases from 10 J/m<sup>2</sup> to 20 J/m<sup>2</sup>, the increment of lattice temperature,  $T_l$ , is about 235K, whereas the increment is only around 52K for  $F$  from 40 J/m<sup>2</sup> to 50 J/m<sup>2</sup>. The increment follows a non-linear trend, as observed in the case of electron temperature.

Moreover, it takes more time for electrons and lattices to get into thermal equilibrium (6 ps to 12 ps) as  $F$  increases from 10 J/m<sup>2</sup> to 50 J/m<sup>2</sup> with an interval of 10 J/m<sup>2</sup>. The main reason behind the decrement of the equilibrium temperature gap and increment of the equilibrium time is that the two Ti nanoparticles get completely melted or amorphous as  $F$  rises from 40 J/m<sup>2</sup> to 50 J/m<sup>2</sup>. The latent heat of melting uses a portion of the laser's energy to compensate for the energy required for melting, which ultimately results in a minor increase of lattice temperature,  $T_l$  and thus prolongs the time needed for the electrons and lattice to achieve thermal equilibrium [78].

In addition, according to Figure 3(b), lattice temperature,  $T_l$  with varied laser pulse width,  $t_p$  nearly overlap one another when  $F$  is set at the melting fluence, 50 J/m<sup>2</sup>. There is a discrete

difference in the time it takes for  $T_e$  to reach its highest value, and the laser irradiation duration solely produces this difference. The more the pulse width,  $t_p$ , the more it takes time for electrons to achieve the maximum temperature. Furthermore, the maximum  $T_e$  decreases as  $t_p$  grows longer. The maximum temperature,  $T_e$ , is reduced because a portion of the energy transferred from the electron subsystem to the lattice subsystem occurs concurrently during femtosecond laser irradiation, an electron-phonon-linked energy transport process. Consequently, as  $t_p$  increases, the impact of electron-phonon coupled energy transfer on lowering maximum  $T_e$  becomes more pronounced and thus, a shorter  $t_p$  results in quicker electron heating [79]. Meanwhile, the lattice temperature remains almost constant while altering the pulse width,  $t_p$ .

**Table 2:** Different combinations of absorbed laser fluence and laser pulse width on the sintering process

Laser fluence, $F(\text{J/m}^2)$	Laser pulse width, $t_p(\text{fs})$
10	100
20	100
30	100
40	100
50 (complete melting)	100
50	10
50	35
50	60
50	150
50	200

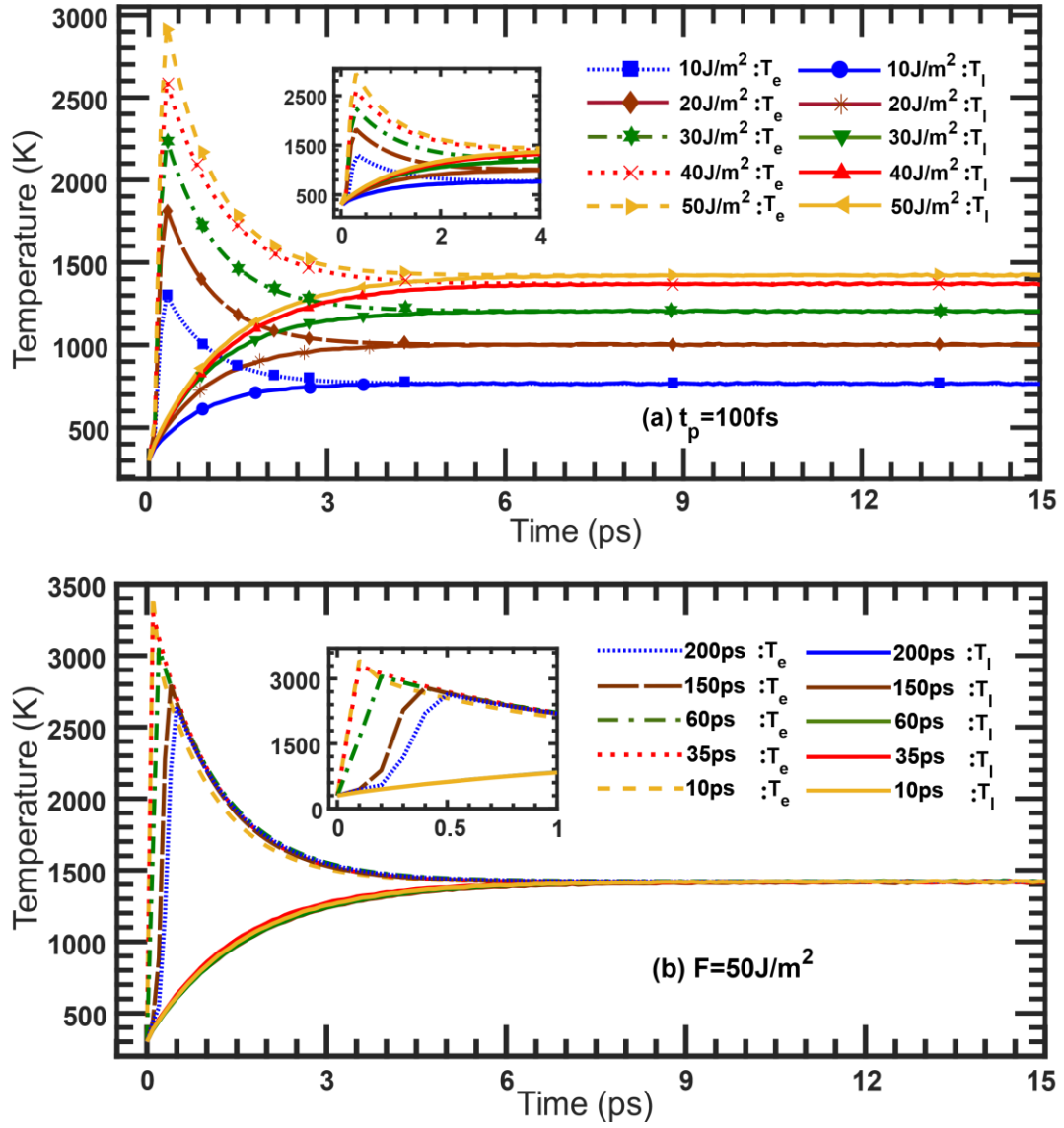


**Figure-3: Temporal evolutions of electron and lattice Temperature at (a) the constant pulse width of 100 fs but different fluence,  $F$  (b) the constant fluence of 50  $\text{J/m}^2$  but different pulse width,  $t_p$**

### 4.3. Visualizing the sintering process from atomistic snapshots

We have already analyzed the temporal evolutions of electron temperature,  $T_e$  and lattice temperature,  $T_l$ , but it is tough to access the nanoscale information of Ti nanoparticles during the sintering process just by seeing the temporal evolutions. That's why atomistic snapshots were taken to visualize the sintering process to a greater extent in Figure 4. At first, Ti nanoparticles were relaxed at room temperature, 298.15K. The most stable phase of both Ti nanoparticles has been shown in Fig:4(a) immediately after the relaxation process. The NVT ensemble was applied during the relaxation process, so the neck is minimal at this point. This marks the point at which femtosecond laser energy begins to irradiate, starting at 0 ps. According to the TTM described earlier, a large amount of laser energy is initially deposited in the electron subsystem in the sub-picosecond time frame. Within a short period, the temperature of the lattice sub-system starts to increase gradually due to electron-phonon coupling. Meanwhile, the Ti lattice maintains FCC structure and vibrates around their positions in Fig:4(a) and Fig:4(b).

Mass transport serves as the fundamental mechanism driving the sintering process. Mass transport arises from the system's drive to decrease the total interface energy and the energy of the particles or grains [80]. It can be found that there is a slight increase in the volume of Ti nanoparticles from Fig:4(a) to Fig:4(c) due to thermal expansion and an increase in the nanoparticle contact area. Mass transport (surface diffusion, volume diffusion) works as the main driving force here [81]. Maximum volume thermal expansion is observed at 1 ps in Fig:4(c). So far, there hasn't been much of an increase in neck width. In the present MD simulation, the canonical NVE ensemble was applied, maintaining the total energy constant. There is no external pressure applied to constrain the thermal expansion. At the point of maximum thermal expansion, the atoms depicted in Figure 4(c) are unable to sustain the FCC lattice structure and gradually begin to deform toward an amorphous shape.

From Fig:4(d), densification between the nanoparticles begins to accelerate as the lattice temperature,  $T_l$ , increases gradually, and the sintering neck, undergoing rapid expansion via mass transport, gradually approaches the particle's diameter, 6nm. At this stage, the nanoparticles contract volumetrically, and the lattice structure deviates from its FCC shape more. The structure becomes completely amorphous at 10 ps in Fig:4(e), which can be called a phase-changing point or melting point for Ti nanoparticles, and the lattice temperature,  $T_l$ , at that point, is 1416K. The lattice temperature becomes stable at 12 ps in Fig:4(f), and the maximum lattice temperature at that point is 1423K. The electron and lattice temperature equilibrates around this temperature from now on and doesn't increase or decrease further according to our observation from temporal evolutions of electron and lattice temperature in Figure 1. Mass transport via inter-grain boundary diffusion is active at this point and as a result neck size increases, approaching the particle diameter of 6nm [82]. The nanoparticles are denser than before, and the densification effect continues, though there is no change in lattice temperature after 12 ps (Fig:4(f)). Afterward, as the simulation progresses, the two Ti nanoparticles merge into a large Ti nanoparticle at 150 ps with the stable minimum surface energy in Fig:4(i) [59, 83, 84].

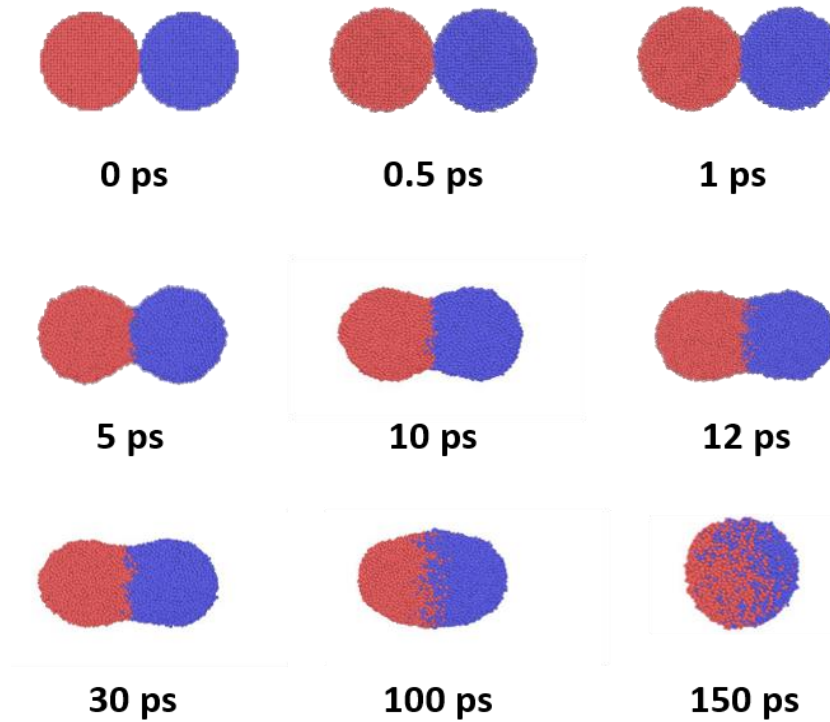


**Figure-4: Atomistic Snapshots of Laser Sintering of Ti nanoparticles**

#### **4.4. Insight into the structural transformation by common neighbor analysis**

An estimate of the melting time may be obtained by analyzing the temporal changes in the Radial distribution function. However, more study is required to ascertain the melting temperature.

The melting temperature is determined by analyzing the plot of the System potential energy ( $E_{\text{pot}}$ ) vs System temperature. The sudden shift in the system's potential energy concerning temperature causes the quick phase transition in this figure. The endpoint of the leap signifies the system's fully amorphous condition, which corresponds to the entire melting state of the system, with the temperature at this point being the melting temperature.

Figure-5 displays the potential energy of the system ( $E_{\text{pot}}$ ) plotted against the lattice curve, along with an analysis of the system's crystal structure coordination. The electronic subsystem heats faster than the lattice subsystem under ultrafast laser irradiation. Following irradiation, the lattice experiences heating caused by the thermal vibrations of atoms due to electron-phonon interaction. The system experiences a localized amorphous state due to fast thermal vibration, which can be verified using coordination analysis.

The surface atoms are in an amorphous condition after 1 ps, when the lattice temperature is around 900 K, whereas the core atoms are mainly in a crystalline state. We noticed that the disordered surface atoms thicken at about 3 ps when the lattice temperature is around 1350K. A quick phase transition phenomenon, indicated by a sharp increase in potential energy after 3 ps, was noted. The coordination study also shows that the core atoms undergo a fast phase transition, during which they lose their crystalline form, and that the abrupt transition concludes at around 10 ps. At that moment, the temperature was around 1416 K. At the very end of the quick leap, the nanoparticle system melted, according to coordination analysis. This further suggests that the melting point is around 1416 K, and the estimated time it takes to melt is 10 ps.

The nanoparticle system had a relatively low melting point compared to the melting point of bulk Ti, which is around 1910 K. The distinctive characteristics of Ti nanoparticles are due to their microscopic size. The surface density grows to outweigh that of the core due to its diminutive size. Because of this, the surface's atomic configuration changes and the strength of the interatomic bond decreases. Therefore, the nanoparticles' melting point is reduced. Because of their diminutive size, nanoparticles have a greater surface-to-volume ratio than bulk materials. More surface area means more surface energy. A lowered nanoparticle melting point is possible due to their high surface energy. Thus, further investigated with respect to the system potential energy concerning temperature, the melting point of the Ti nanoparticle

system is around 1416 K which closely aligns with the prior research for the 6 nm titanium nanoparticles [38, 39].

Additionally, the results of this research also corroborate the approximation of the melting time that we discovered while analyzing the radial distribution function (RDF).

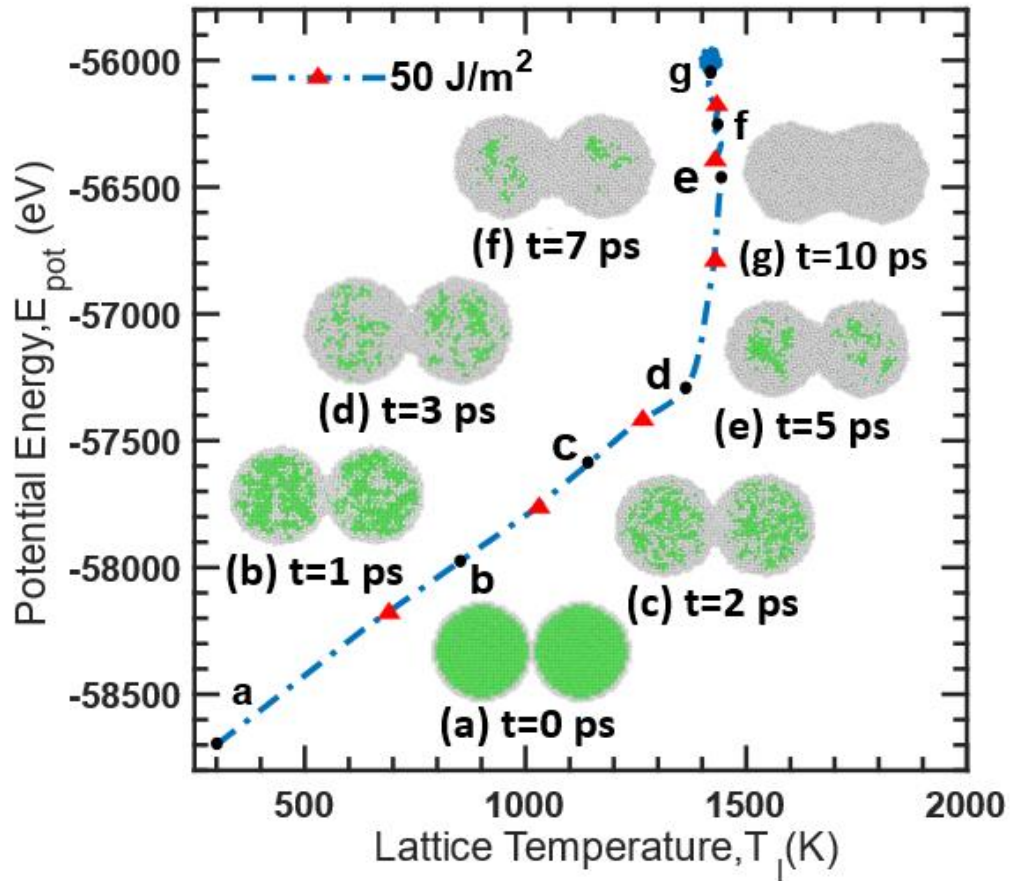


**Figure-5: Potential Energy Variation with Lattice Temperature at 50J/m<sup>2</sup> fluence and 100 fs pulse width**



## 4.5. Amorphous Rate:

Amorphous rate refers to the speed or rate at which a material transforms from a crystalline structure to an amorphous structure. When a material undergoes amorphous transformation, its atoms or molecules lose their ordered arrangement characteristic of a crystalline structure and instead adopt a disordered, random arrangement typical of an amorphous structure. When a material is subjected to high fluence, the energy deposition can cause significant atomic displacement and disruption of the crystalline lattice structure. This disruption can lead to the formation of defects, vacancies, and ultimately an amorphous state.

In the figure, we observe that at higher fluence the amorphous rate is also higher. This is because at higher fluence a greater amount of energy is available to induce atomic rearrangements and disorder.

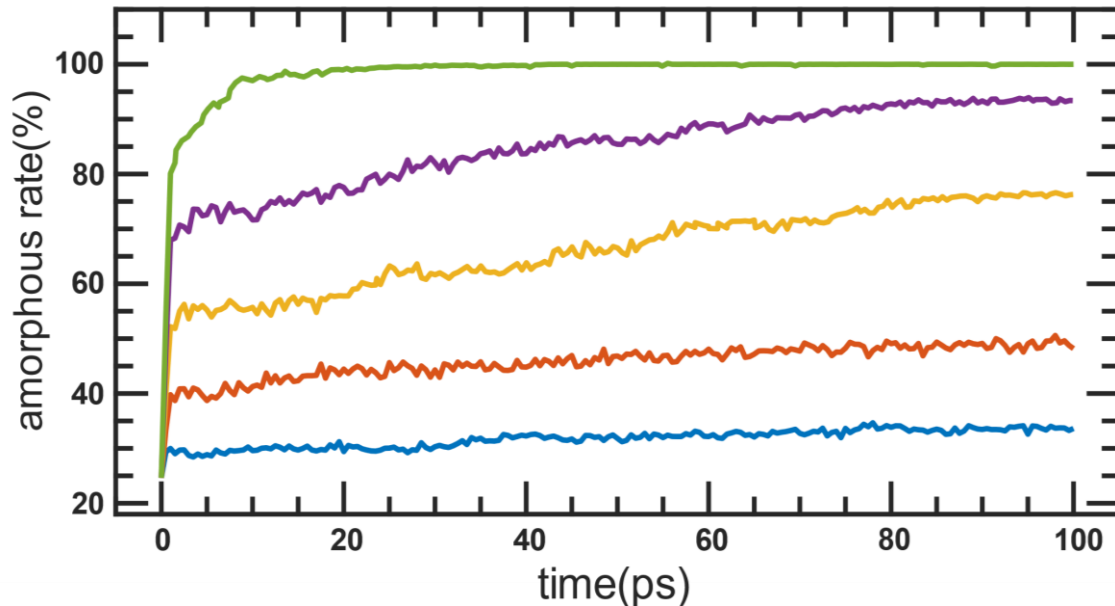


**Figure-6: Amorphous Rate with Time at constant pulse width of 100 fs for different laser fluences (i) 10 J/m<sup>2</sup> (Blue) (ii) 20 J/m<sup>2</sup> (Orange) (iii) 30 J/m<sup>2</sup> (Yellow) (iv) 40 J/m<sup>2</sup> (Purple) (v) 50 J/m<sup>2</sup> (Green)**

## 4.6. Sintering parameters

### 4.6.1. Radial Distribution Function (RDF)

Radial Distribution Function (RDF) is a pair correlation function, which describes how the atoms in a system, on average, are packed together in a system. RDF is calculated considering a series of concentric spheres around an atom with the spheres set at  $\Delta r$  apart and using the following formula.

$$g(r) = \frac{n(r)}{\rho 4\pi r^2 \Delta r}$$

where,  $g(r)$  is the RDF,  $n(r)$  is the mean number of atoms in a shell of width  $\Delta r$  at distance  $r$ ,  $\rho$  is the mean atom density.

In the initial stage, the RDF reveals distinct peaks at specific distances, notably at 3Å, 4.2Å, 5.2Å, and 5.8Å. These pronounced peaks correspond to the characteristic structure of face-centered cubic (FCC) arrangements within the Ti nanoparticles. The sharpness and prominence of these peaks signify the crystalline nature of the system.

Upon laser heating, the RDF profile undergoes significant alterations indicative of structural transformation. As the thermal energy imparted by the laser induces atomic motion, the crystalline lattice of Ti nanoparticles begins to disintegrate. This is manifested by a gradual decrease in peak height and broadening of peak widths in the RDF graph. The diminishing peak heights signify a reduction in the degree of atomic ordering, reflecting the progressive amorphization of the system.

During the sintering process, characterized by intense interparticle interactions and fusion, the RDF profile undergoes further modifications. The disappearance of distinct peaks in the RDF graph signifies the loss of long-range crystalline order, indicative of the formation of a non-crystalline, amorphous phase. The absence of sharp peaks underscores the homogenization of atomic distributions within the sintered Ti nanoparticles.

The graph we obtained matches with the existing works on RDF [57, 85].

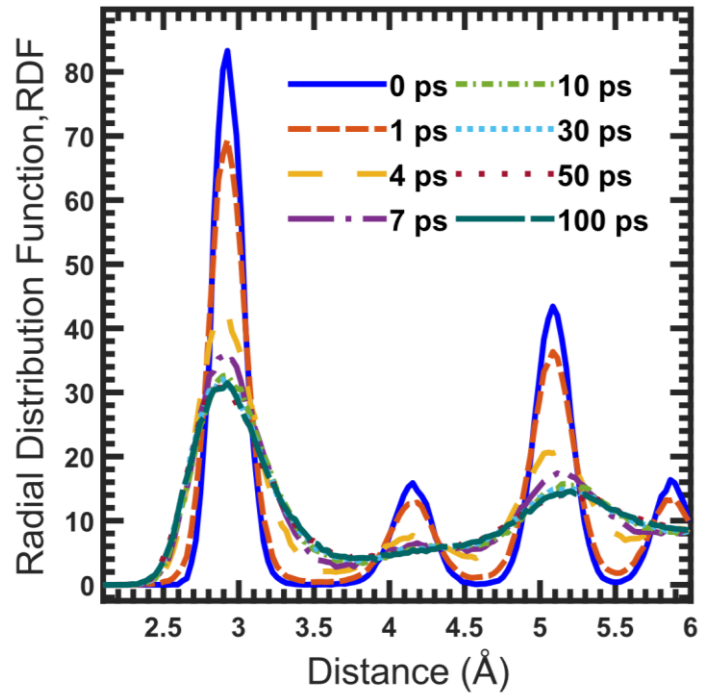


**Figure-7: RDF of Ti NPs at different temporal points  
at 50J/m<sup>2</sup> fluence and 100 fs pulse width**

#### 4.6.2. Mean Square Displacement (MSD)

As molecules in a system move, they collide with each other after certain distances. The distances travelled by the molecules before collision are random. The average square distance taken over all the molecules in the system is Mean Square Displacement (MSD). MSD can be calculated using the following expression.

$$MSD = \frac{1}{N} \sum_{i=1}^N [x_i(t) - x_i(0)]^2$$

Where,

$N$  = the total number of atoms

$x_i(t)$  = the displacement of the atom  $i$  at time

$x_i(0)$  = the displacement of the atom  $i$  at the initial time

Laser fluence determines the amount of energy delivered per unit area. When the fluence increases, more energy is absorbed by the Ti nanoparticles, leading to more significant heating and enhanced particle motion. The absorbed energy translates directly into kinetic energy for the particles, increasing their displacement. That's why we observe increasing MSD values with increasing laser fluence [37].

The pulse width affects the rate at which energy is delivered but not the total energy absorbed since the fluence is constant. For ultra-short pulses, the energy is delivered almost instantaneously, whereas for longer pulses, the energy is spread out over a slightly longer duration. However, for the pulse widths considered, the time scales are still very short, and the rapid energy distribution means there is little time for thermal diffusion to occur during the pulse duration. As a result, there are negligible variations in the graph with varying pulse width.

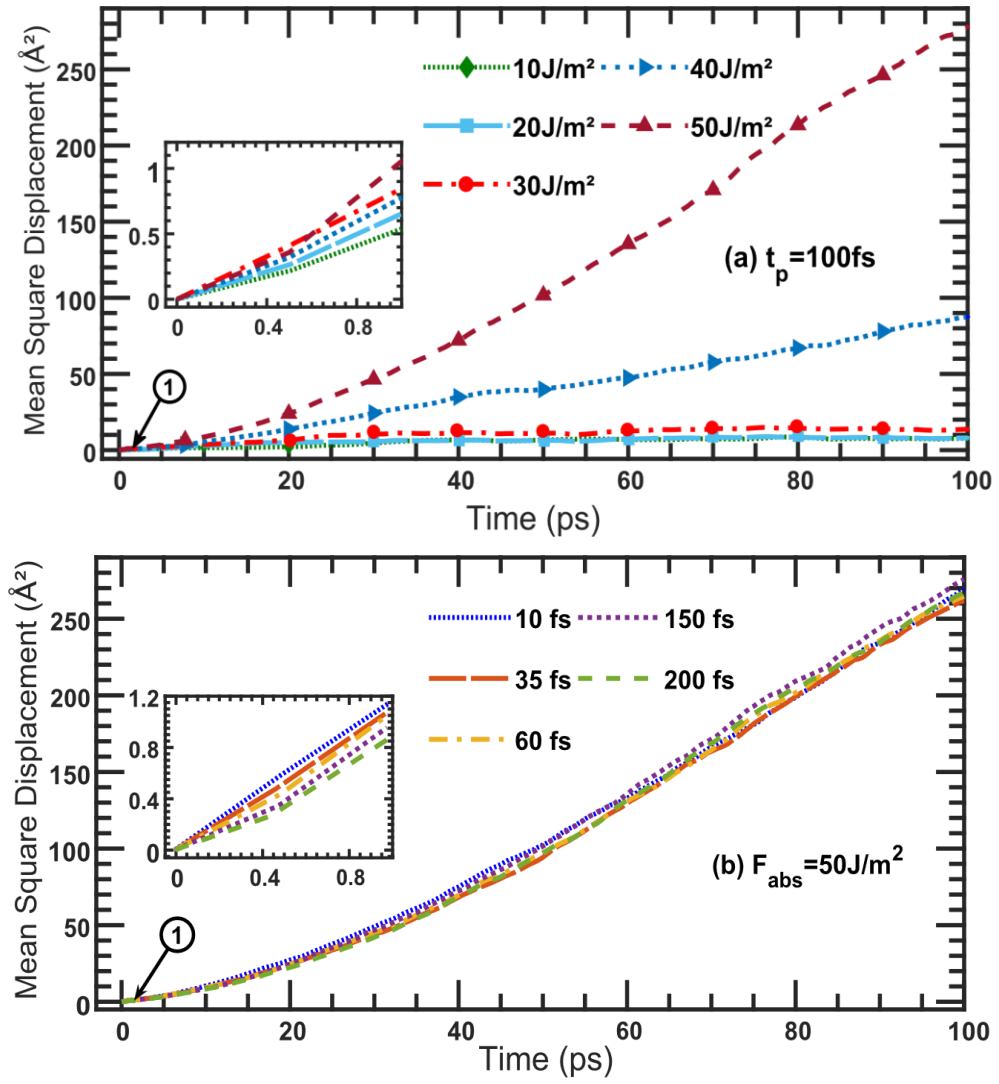


**Figure-8: Mean Square Displacement (MSD) variation with time at (a) constant pulse width 100 fs and (b) constant fluence 50  $\text{J/m}^2$**

### 4.6.3. Radius of Gyration

The radius of gyration quantifies how mass is distributed inside a molecule in space. It details the molecule's general structure and dimensions about its mass distribution. It provides insights about the density or size of the molecular structure.

The radius of gyration  $R_{gyr}$  is calculated from,

$$R_{gyr} = \sqrt{\frac{1}{M} \sum_{i=1}^N m_i (r_i - r_{com})^2}$$

where  $M$  is the total mass of atoms in the simulation system,  $N$  is the total number of atoms,  $m_i$  is the mass of atom  $i$ ,  $r_i$  is the position of the atom  $i$  and  $r_{com}$  is the center of mass position.

It can be seen that the curves of  $R_{gyr}$  and  $\varepsilon$  exhibit contrasting tendencies. Before reaching 1ps, during the first stage, the  $R_{gyr}$  slowly rises and peaks owing to the thermal expansion of the two Ti nanoparticles. During the second stage, when the Ti nanoparticles sinter and condense into a new Ti nanoparticle, there is a fast decrease in  $R_{gyr}$ . The rapid decrease in radius of gyration indicates a significant stage in the sintering process of titanium nanoparticles. As these nanoparticles undergo melting, they develop sintered necks, characterized by intense interparticle interactions. This leads to the formation of bridges between adjacent nanoparticles, causing an abrupt elevation in strain as fusion kinetics accelerate during this phase. As fusion continues, the change in radius of gyration diminishes, signaling the consolidation of nanoparticles into a larger entity [57].

The effect of pulse width variation at constant laser fluence on radius of gyration is negligible. The reason is explained in the section 4.7.

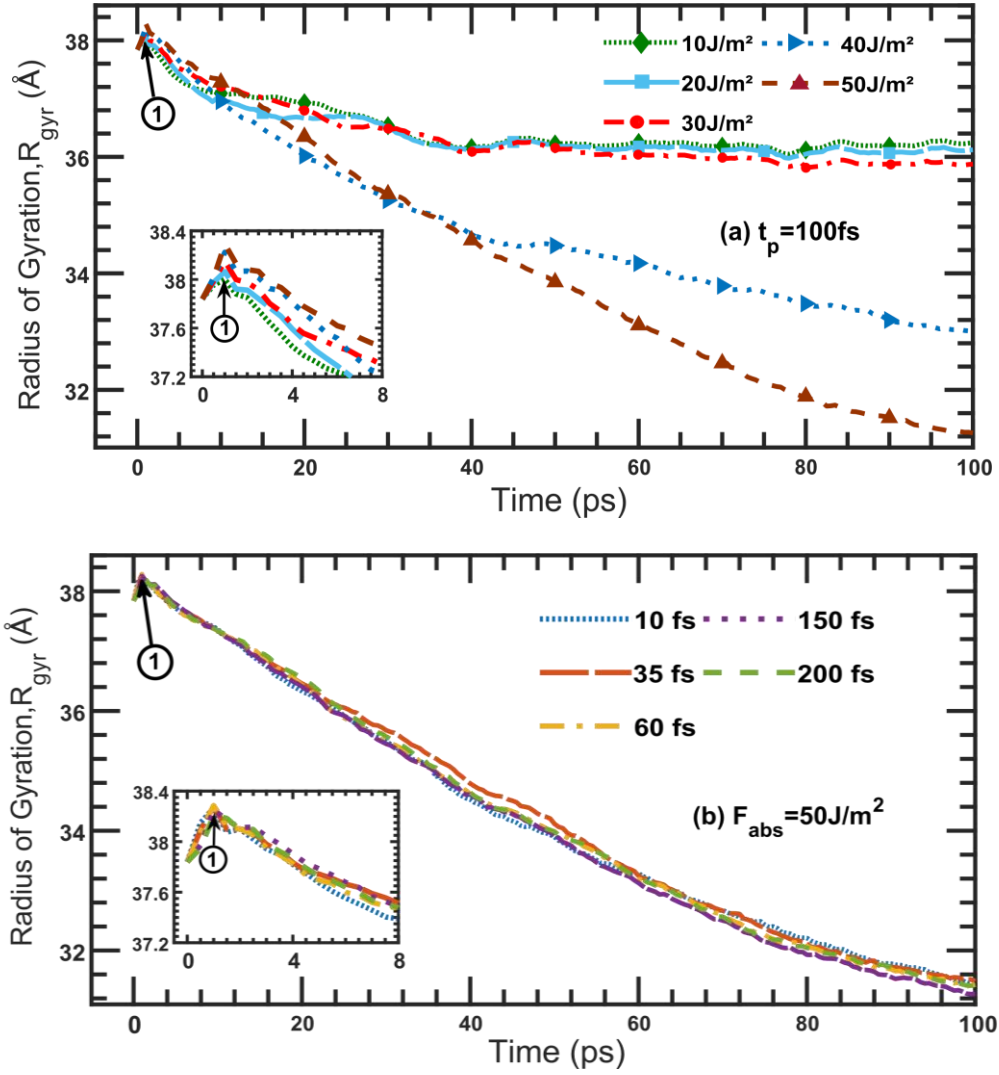


**Figure-9: Radius of Gyration variation with time at (a) constant pulse width 100 fs and (b) constant fluence 50 J/m²**

#### 4.6.4. Shrinkage Ratio

The shrinkage ratio,  $\varepsilon$  is calculated from the following equation,

$$\varepsilon = \frac{l_0 - l_t}{l_0}$$

where  $l_0$  and  $l_t$  represent the distances between the centers of Ti nanoparticles at the initial moment and at a given temporal point  $t$ , respectively.

Initially,  $\varepsilon$  experiences a marginal decline attributed to thermal expansion induced by femtosecond laser heating. This phase, occurring within the first picosecond, sets the stage for subsequent transformations by priming the nanoparticles for fusion.

The subsequent rapid increase in  $\varepsilon$  signifies the development of sintered necks as Ti nanoparticles undergo melting. This stage is characterized by intense interparticle interactions, leading to the formation of bridges between adjacent nanoparticles. The abrupt elevation in  $\varepsilon$  reflects the accelerated kinetics of fusion during this phase.

As the fusion progresses, the rate of  $\varepsilon$  growth diminishes, indicating the consolidation of nanoparticles into larger entities. Notably, the formation of a single large Ti nanoparticle is accompanied by non-uniform distribution of Ti atoms within the resultant structure. This heterogeneity in atomic arrangement contributes to the observed plateauing of  $\varepsilon$  growth, as the random motions of Ti atoms within the fused nanoparticle gradually dominate the dynamics [57].

The effect of pulse width variation at constant fluence on shrinkage ratio is negligible. The reason is explained in the section **4.7**.



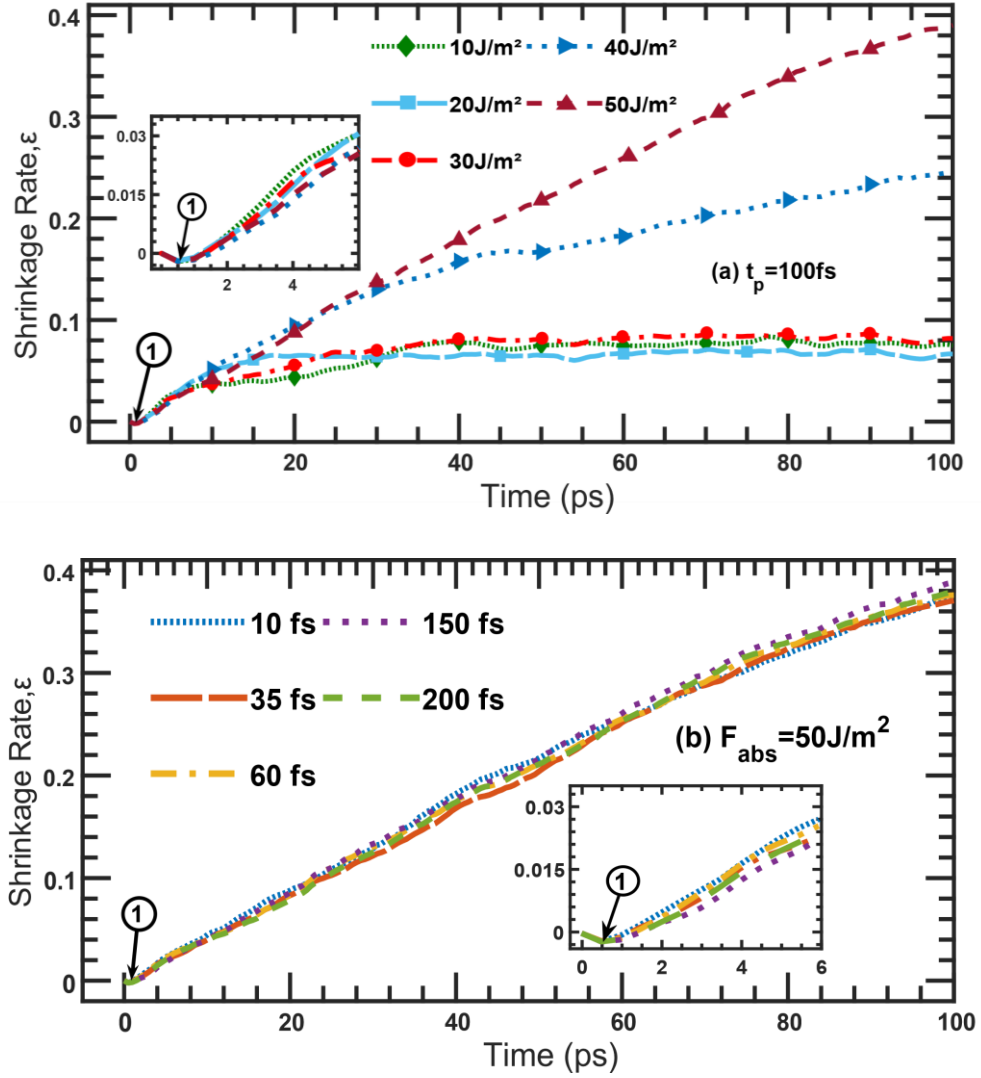


**Figure-10: Shrinkage Ratio variation with time at (a) constant pulse width 100 fs and (b) constant fluence  $50 \text{ J/m}^2$**

#### 4.6.5. Neck Radius:

As sintering progresses, neck formation is observed between the two Ti NPs. At higher fluence, the rate of neck formation is higher. The reasons for this are increased energy absorption by the surface, enhanced particle motion and accelerated particle motion. Higher fluence means more energy is being deposited into the system. This increased energy can lead to more rapid melting and rearrangement of particles, promoting the formation of larger necks between particles. Due to increased energy, the particles oscillate rapidly, resulting in a faster growth rate of the neck radius. Surface diffusion, which involves the movement of atoms or molecules along the surface of particles, is essential for neck formation during sintering. At higher fluence levels, the increased energy can enhance surface diffusion rates, facilitating the coalescence of particles and neck formation [86].

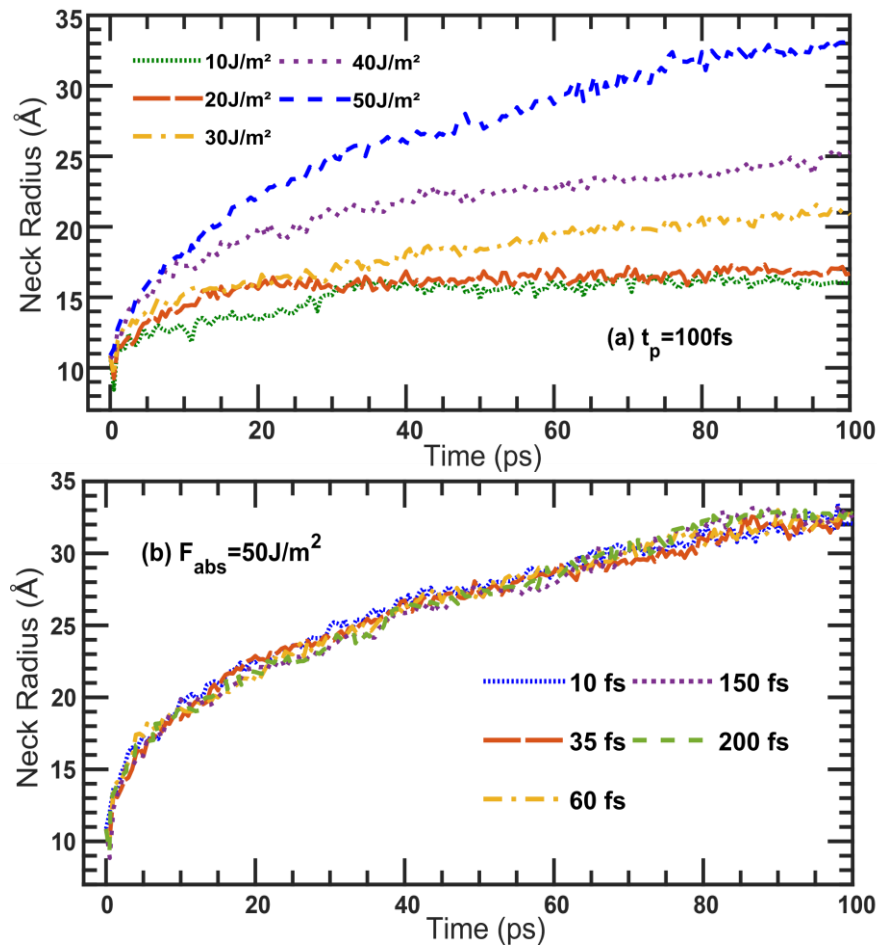


**Figure-11: Neck Radius variation with time at (a) constant pulse width 100fs and (b) constant fluence  $50\text{ J/m}^2$**

## **4.7. Effect of pulse width variation in sintering parameters:**

In the study of laser sintering of nanoparticles using femtosecond lasers, a key finding is that certain sintering parameters vary negligibly as the pulse width varies when the laser fluence is constant. This can be explained by how energy is deposited and how the material responds during sintering with femtosecond lasers.

Femtosecond lasers emit very short pulses of energy, resulting in high peak power. This means a large amount of energy is quickly deposited into the material, causing rapid heating with minimal heat spreading to surrounding areas. When fluence is kept constant, the total energy delivered to the nanoparticles stays the same, regardless of the pulse width.

In the femtosecond-picosecond range, the energy deposition occurs on timescales shorter than or comparable to the electron-phonon relaxation time (typically in the order of femtoseconds). This means that the energy is rapidly absorbed by the electrons, leading to highly localized heating and subsequent non-thermal processes such as multiphoton ionization and avalanche ionization. These processes are highly nonlinear and occur almost instantaneously with the laser pulse, resulting in similar material responses regardless of slight variations in pulse width within the femtosecond-picosecond range [87]. The ultrafast deposition of energy in this timescale limits thermal diffusion during the pulse, confining the energy to a very small volume. The heat affected zone is highly localized, and the interaction is dominated by electronic excitation and subsequent rapid thermalization.

Non-thermal processes such as multiphoton ionization and avalanche ionization dominate in this regime. These processes are largely independent of the pulse width because the energy is delivered so quickly that the primary mechanisms are related to electronic excitation and bond breaking, which occur on ultrafast timescales.

Since thermal diffusion is minimal during the pulse, variations in pulse width do not significantly affect the localized heating and the subsequent material dynamics. As a result, the material modification is primarily governed by these ultrafast processes, leading to similar MSD and other parameters regardless of small changes in pulse width.

In the nanosecond range, the pulse duration is much longer, allowing for thermal diffusion to play a significant role. The energy deposition occurs over a longer period, enabling heat to diffuse away from the interaction zone, leading to more uniform and less localized heating.

Variations in pulse width in the nanosecond range can significantly alter the thermal profile and energy distribution within the material, resulting in noticeable changes in MSD and other sintering parameters [88].

In summary, the lack of effect of pulse width variation on MSD and other parameters in the femtosecond-picosecond range is due to the dominance of non-thermal, highly localized processes and minimal thermal diffusion during the pulse. In the nanosecond range, thermal processes and heat conduction play a significant role, and variations in pulse width lead to different thermal profiles and material responses, resulting in noticeable changes in sintering parameters.

## 5. Conclusion:

This study elucidates the distinct effects of laser heating on the sintering of titanium nanoparticles, differing significantly from uniform heating methods. By using TTM, we effectively simulate the rapid dynamics of laser-induced heating processes in the electron and lattice subsystem. Besides, melting temperature via structural transformation of nanoparticles has been investigated. Our detailed analysis reveals several key observations:

**Mean Squared Displacement (MSD):** As sintering progresses, the MSD of the Ti nanoparticles increase continuously, indicating ongoing diffusion and particle movement. Higher laser fluence results in greater MSD values, reflecting enhanced particle dynamics due to more intense energy input. Notably, MSD remains unaffected by variations in pulse width.

**Radius of Gyration:** Initially, the radius of gyration increases due to thermal expansion. However, as sintering advances, the fusion of the two nanoparticles causes a decrease in the radius of gyration. Higher laser fluence accelerates this reduction, indicating more efficient particle coalescence. Similar to MSD, the radius of gyration does not vary with changes in pulse width, reinforcing the role of fluence in driving the sintering process. Radius of gyration remains unaffected by variations in pulse width.

**Shrinkage Ratio:** The evolution of  $\epsilon$  during femtosecond laser-induced sintering shows an initial decline due to thermal expansion, followed by a rapid increase indicating sintered neck development and intense interparticle interactions. Eventually,  $\epsilon$  growth stabilizes as nanoparticles consolidate into a sintered particle. Shrinkage ratio remains unaffected by variations in pulse width.

Radial Distribution Function (RDF): The RDF curves obtained in this study match well with existing RDF curves in the literature, affirming the accuracy of our simulation approach. The RDF provides insights into the gradual amorphization during sintering.

Neck Radius: As sintering progresses, higher fluence levels result in accelerated neck formation between Ti nanoparticles due to increased energy absorption, enhanced particle motion, and accelerated surface diffusion, leading to more rapid melting and rearrangement of particles and promoting the formation of larger necks between particles. It remains unaffected by variations in pulse width.

The study offers valuable understanding of the laser sintering mechanisms of Ti nanoparticles. Future work should explore the role of other parameters, such as nanoparticle size and laser wavelength, to further refine sintering techniques.

## References:

1. Bert Huis in 't, V., et al., *Micro additive manufacturing using ultra short laser pulses*. CIRP Annals, 2015. **64**(2): p. 701-724.
2. Wong, K.V. and A. Hernandez, *A Review of Additive Manufacturing*. ISRN Mechanical Engineering, 2012. **2012**: p. 1-10.
3. Zhao, C., P.J. Shah, and L.J. Bissell, *Laser additive nano-manufacturing under ambient conditions*. Nanoscale, 2019. **11**(35): p. 16187-16199.
4. R.R.Boyer, *An overview on the use of titanium in the aerospace industry*. Materials Science and Engineering, 1996.
5. Froes, F.H., *Titanium for medical and dental applications—An introduction*, in *Titanium in Medical and Dental Applications*. 2018. p. 3-21.

6. Allison, A.M.S.a.J.E., *Potential for Automotive Applications of Titanium Alloys*. SAE Transactions, 1986. **95**: p. 806-817.
7. E.O. Ezugwu, Z.M.W., *Titanium alloys and their machinability—a review*. Journal of Materials Processing Technology, 1997. **68**(3): p. 262-274.
8. Celestino VeigaJ, P.D., LoureiroA, *Properties and applications of titanium alloys: A brief review*. Reviews on Advanced Materials Science, 2012. **32**(2): p. 133-148.
9. Tanisha Pereiraa, J.V.K., Johan Potgieter *A comparison of traditional manufacturing vs additive manufacturing, the best method for the job*. Procedia Manufacturing, 2019. **30**: p. 11-18.
10. Kurian, S. and R. Mirzaeifar, *Selective laser melting of aluminum nano-powder particles, a molecular dynamics study*. Additive Manufacturing, 2020. **35**.
11. Cheng, C.-W., et al., *Femtosecond laser melting of silver nanoparticles: comparison of model simulations and experimental results*. Applied Physics A, 2018. **124**(5).
12. Wang, X.C., et al., *Direct Selective Laser Sintering of Hard Metal Powders: Experimental Study and Simulation*. The International Journal of Advanced Manufacturing Technology, 2002. **19**(5): p. 351-357.
13. Song, Y.-A. and W. Koenig, *Experimental Study of the Basic Process Mechanism for Direct Selective Laser Sintering of Low-Melting Metallic Powder*. CIRP Annals, 1997. **46**(1): p. 127-130.
14. Goudeli, E. and S.E. Pratsinis, *Crystallinity dynamics of gold nanoparticles during sintering or coalescence*. AIChE Journal, 2016. **62**(2): p. 589-598.
15. Musazadeh, M.H. and K. Dehghani, *The Effect of Crystallographic Orientation on Sintering Behavior of Ni Nanoparticles: A Molecular Dynamic Study*. Journal of Computational and Theoretical Nanoscience, 2013. **10**(6): p. 1497-1502.

16. Cheng, C.W. and J.K. Chen, *Femtosecond laser sintering of copper nanoparticles*. Applied Physics A, 2016. **122**(4).
17. Hu, Q., et al., *Additive manufacture of complex 3D Au-containing nanocomposites by simultaneous two-photon polymerisation and photoreduction*. Sci Rep, 2017. **7**(1): p. 17150.
18. S. Maruo, S.K., *Two-Photon-Absorbed Near-Infrared Photopolymerization for Three-Dimensional Microfabrication*. Journal of Microelectromechanical Systems, 1998.
19. Zheng, X., et al., *Design and optimization of a light-emitting diode projection micro-stereolithography three-dimensional manufacturing system*. Rev Sci Instrum, 2012. **83**(12): p. 125001.
20. Sun, C., et al., *Projection micro-stereolithography using digital micro-mirror dynamic mask*. Sensors and Actuators A: Physical, 2005. **121**(1): p. 113-120.
21. Ware, H.O.T. and C. Sun, *Method for Attaining Dimensionally Accurate Conditions for High-Resolution Three-Dimensional Printing Ceramic Composite Structures Using MicroCLIP Process*. J Micro Nanomanuf, 2019. **7**(3): p. 0310011-3100110.
22. Han, Y., C. Wei, and J. Dong, *Droplet formation and settlement of phase-change ink in high resolution electrohydrodynamic (EHD) 3D printing*. Journal of Manufacturing Processes, 2015. **20**: p. 485-491.
23. Han, Y. and J. Dong, *Design of Integrated Ring Extractor for High Resolution Electrohydrodynamic (EHD) 3D Printing*. Procedia Manufacturing, 2016. **5**: p. 1031-1042.
24. Nagarajan, B., et al., *Development of Micro Selective Laser Melting: The State of the Art and Future Perspectives*. Engineering, 2019. **5**(4): p. 702-720.



25. Li, J. and M. Pumera, *3D printing of functional microrobots*. Chem Soc Rev, 2021. **50**(4): p. 2794-2838.
26. Lee, Y.W., et al., *3D-Printed Multi-Stimuli-Responsive Mobile Micromachines*. ACS Appl Mater Interfaces, 2021. **13**(11): p. 12759-12766.
27. Sun, K., et al., *3D printing of interdigitated Li-ion microbattery architectures*. Adv Mater, 2013. **25**(33): p. 4539-43.
28. Kwon-Hyung Lee, S.-S.L., David B. Ahn, *Ultrahigh areal number density solid-state on-chip microsupercapacitors via electrohydrodynamic jet printing*. Science Advances, 2020.
29. Nseowo Udofia, E. and W. Zhou, *3D printed optics with a soft and stretchable optical material*. Additive Manufacturing, 2020. **31**.
30. Ding, A., et al., *4D biofabrication via instantly generated graded hydrogel scaffolds*. Bioact Mater, 2022. **7**: p. 324-332.
31. Yang, L., et al., *Molecular dynamics simulation of neck growth in laser sintering of different-sized gold nanoparticles under different heating rates*. Applied Physics A, 2011. **106**(3): p. 725-735.
32. Zhang, Y. and J. Zhang, *Sintering phenomena and mechanical strength of nickel based materials in direct metal laser sintering process—a molecular dynamics study*. Journal of Materials Research, 2016. **31**(15): p. 2233-2243.
33. Yang, Y., et al., *Multiscale simulation study of laser sintering of inkjet-printed silver nanoparticle inks*. International Journal of Heat and Mass Transfer, 2020. **159**.
34. Huang, P.-H., et al., *Laser sintering of Cu nanoparticles: analysis based on modified continuum-atomistic model*. Applied Physics A, 2019. **126**(1).
35. Nandy, J., H. Sarangi, and S. Sahoo, *A Review on Direct Metal Laser Sintering: Process Features and Microstructure Modeling*. Lasers in Manufacturing and Materials Processing, 2019. **6**(3): p. 280-316.

36. Nandy, J., et al., *Sintering of AlSi10Mg particles in direct metal laser sintering process: A molecular dynamics simulation study*. Materials Chemistry and Physics, 2019. **236**.
37. Nandy, J., et al., *Molecular dynamics simulation of coalescence kinetics and neck growth in laser additive manufacturing of aluminum alloy nanoparticles*. J Mol Model, 2020. **26**(6): p. 125.
38. Rahmani, F., et al., *Melting and solidification behavior of Cu/Al and Ti/Al bimetallic core/shell nanoparticles during additive manufacturing by molecular dynamics simulation*. Journal of Nanoparticle Research, 2018. **20**(5).
39. Jeon, J., et al., *Molecular dynamics study of temperature and heating rate–dependent sintering of titanium nanoparticles and its influence on the sequent tension tests of the formed particle-chain products*. Journal of Nanoparticle Research, 2020. **22**(1).
40. Ling-Feng Lai, D.-M.L., Chun-Hsien Li, Kun-Hsien Chen, Shun-Chang Lin, Yu-Chen Su, Shan and D.-S.L. Jiang, Kuei-Shu Hsu, Jian-Ming Lu , Ming-Hsiao Lee,Zhen Chen, *Physical Characteristics of Nanoscale Titanium-Aluminum Alloy Powder during 3D Printing Laser Sintering Process - A Molecular Dynamics Study*. 2018.
41. Koparde, V.N. and P.T. Cummings, *Sintering of titanium dioxide nanoparticles: a comparison between molecular dynamics and phenomenological modeling*. Journal of Nanoparticle Research, 2008. **10**(7): p. 1169-1182.
42. Dal Forno, S. and J. Lischner, *Electron-phonon coupling and hot electron thermalization in titanium nitride*. Physical Review Materials, 2019. **3**(11).
43. Attar, H., et al., *Manufacture by selective laser melting and mechanical behavior of commercially pure titanium*. Materials Science and Engineering: A, 2014. **593**: p. 170-177.

44. Ik-Hyun Oh, N.N., Shuji Hanada, *Microstructures and Mechanical Properties of Porous Titanium Compacts Prepared by Powder Sintering* Materials Transactions, 2001.
45. Nandy, J., S. Sahoo, and H. Sarangi, *Study on shape dependency of Al-alloy nanoparticles during coalescence in direct metal laser sintering: A molecular dynamics approach*. Materials Today: Proceedings, 2021. **41**: p. 347-351.
46. Malti, A., A. Kardani, and A. Montazeri, *An insight into the temperature-dependent sintering mechanisms of metal nanoparticles through MD-based microstructural analysis*. Powder Technology, 2021. **386**: p. 30-39.
47. Li, Q., et al., *Molecular dynamics simulations of aggregation of copper nanoparticles with different heating rates*. Physica E: Low-dimensional Systems and Nanostructures, 2017. **90**: p. 137-142.
48. P. Zeng, S.Z., P.C. Clapp, J.A. Rifkin, *Nanoparticle sintering simulations*. Materials Science and Engineering, 1998.
49. Shankar Krishnan , J.Y.M., Suresh V. Garimella, *A Two-Temperature Model for Solid-Liquid Phase Change in Metal Foams*. IOP Conference Series: Materials Science and Engineering, 2005.
50. S.I. Anisimov, B.L.K., *Electron emission from metal surfaces exposed to ultrashort laser pulses*. Journal of Experimental theoretical Physics, 1974.
51. Norman, G.E., et al., *Atomistic Modeling of Warm Dense Matter in the Two-Temperature State*. Contributions to Plasma Physics, 2013. **53**(2): p. 129-139.
52. Nicarel, A., et al., *Fourier two-temperature model to describe ultrafast laser pulses interaction with metals: A novel mathematical technique*. Physics Letters A, 2021. **392**.

53. Jiang, L. and H.-L. Tsai, *Improved Two-Temperature Model and Its Application in Ultrashort Laser Heating of Metal Films*. Journal of Heat Transfer, 2005. **127**(10): p. 1167-1173.
54. Carpenne, E., *Ultrafast laser irradiation of metals: Beyond the two-temperature model*. Physical Review B, 2006. **74**(2).
55. Ivanov, D.S. and L.V. Zhigilei, *Combined atomistic-continuum modeling of short-pulse laser melting and disintegration of metal films*. Physical Review B, 2003. **68**(6).
56. Yuwen Zhang, J.K.C., *Ultrafast melting and resolidification of gold particle irradiated by pico- to femtosecond lasers*. Journal of Applied Physics, 2008.
57. Guo, J., et al., *Femtosecond laser sintering Al nanoparticles: A multiscale investigation of combined molecular dynamics simulation and two-temperature model*. Powder Technology, 2022. **407**.
58. Chen, J.K., D.Y. Tzou, and J.E. Beraun, *A semiclassical two-temperature model for ultrafast laser heating*. International Journal of Heat and Mass Transfer, 2006. **49**(1-2): p. 307-316.
59. J.K. Chen, W.P.L., J.E. Beraun, *The role of electron-phonon coupling in ultrafast laser heating*. JOURNAL OF LASER APPLICATIONS, 2005.
60. Alder, B. J. Wainwright, *Studies in Molecular Dynamics. I. General Method*. The Journal of Chemical Physics, 1959. **31**(2): p. 459-466.
61. Rahman, *Correlations in the Motion of Atoms in Liquid Argon*. Physical Review, 1964. **136**(2A): p. A405-A411.
62. Grønbech-Jensen, Niels Farago, *A simple and effective Verlet-type algorithm for simulating Langevin dynamics*. Molecular Physics, 2013. **111**(8): p. 983-991.

63. Zhang, L., G. Hong, and S. Cai, *Molecular dynamics simulation of aggregation of monocrystal and polycrystal copper nanoparticles*. International Journal of Modern Physics B, 2019. **33**(16).
64. Grubmüller, H., et al., *Generalized Verlet Algorithm for Efficient Molecular Dynamics Simulations with Long-range Interactions*. Molecular Simulation, 1991. **6**(1-3): p. 121-142.
65. Wang, Y., X. Ruan, and A.K. Roy, *Two-temperature nonequilibrium molecular dynamics simulation of thermal transport across metal-nonmetal interfaces*. Physical Review B, 2012. **85**(20).
66. Lin, Z., L.V. Zhigilei, and V. Celli, *Electron-phonon coupling and electron heat capacity of metals under conditions of strong electron-phonon nonequilibrium*. Physical Review B, 2008. **77**(7).
67. D. Rakic', B.D.i., *Optical properties of metallic films for vertical-cavity optoelectronic devices*. Applied Optics, 1998. **32**: p. 5271-5283.
68. Xiong, S., et al., *Size- and temperature-induced phase transformations of titanium nanoparticles*. EPL (Europhysics Letters), 2011. **93**(6).
69. S. Daw, M.F., *The embedded-atom method: a review of theory and applications* Materials Science Reports, 1993. **9**(7-8): p. 251-310.
70. Zhou, X.W., R.A. Johnson, and H.N.G. Wadley, *Misfit-energy-increasing dislocations in vapor-deposited CoFe/NiFe multilayers*. Physical Review B, 2004. **69**(14).
71. Plimpton, S., *Fast Parallel Algorithms for Short- Range Molecular dynamics*. Journal of Computational Physics, 1995.
72. Stukowski, Alexander, *Visualization and analysis of atomistic simulation data with OVITO—the Open Visualization Tool*. Modelling and Simulation in Materials Science and Engineering, 2010. **18**(1).

73. Lennard-Jones, J. E, *On the determination of molecular fields. —II. From the equation of state of a gas*. Proceedings of the Royal Society of London. Series A,1997. **106**(738): p. 463-477.
74. Tersoff, J., *New empirical approach for the structure and energy of covalent systems*. Phys Rev B Condensed Matter,1988. **37**(12): p. 6991-7000.
75. Ginibre, Jean, *Statistical Ensembles of Complex, Quaternion, and Real Matrices*. Journal of Mathematical Physics,1965. **6**(3): p. 440-449.
76. Hirel, Pierre, *Atomsk: A tool for manipulating and converting atomic data files*. Computer Physics Communications,2015. **197**: p. 212-219.
77. Wang, N., S.I. Rokhlin, and D.F. Farson, *Ultrafast laser melting of Au nanoparticles: atomistic simulations*. Journal of Nanoparticle Research, 2011. **13**(10): p. 4491-4509.
78. Beaurepaire, E., *Ultrafast Spin Dynamics in Ferromagnetic Nickel*. PHYSICAL REVIEW LETTERS, 1996. **76**.
79. Mo, M.Z., et al., *Determination of the electron-lattice coupling strength of copper with ultrafast MeV electron diffraction*. Rev Sci Instrum, 2018. **89**(10): p. 10C108.
80. German, R.M., *Powder Metallurgy Science*. 1994: Metal Powder Industries Federation.
81. Kang, S.-J.L., *Sintering: densification, grain growth and microstructure*. 2004: Elsevier.
82. Coble, R., *A model for boundary diffusion controlled creep in polycrystalline materials*. Journal of applied physics, 1963. **34**(6): p. 1679-1682.
83. J.S.Raut, *SINTERING OF ALUMINUM NANOPARTICLES:A MOLECULAR DYNAMICS STUDY*. NanoStructured Materials, 1998. **10**(837-851).

84. Ding, L., R.L. Davidchack, and J. Pan, *A molecular dynamics study of sintering between nanoparticles*. Computational Materials Science, 2009. **45**(2): p. 247-256.
85. Zhang, L., et al., *Molecular Dynamics Simulation of the Cu/Au Nanoparticle Alloying Process*. Journal of Nanomaterials, 2019. **2019**: p. 1-7.
86. Hejmady, *Laser sintering of polymer particle pairs studied by in situ visualization*. Soft Matter, 2019. **15**(6): p. 1373-1387.
87. Jeon, Jin-Woo Yoon, *The Effect of Laser Pulse Widths on Laser—Ag Nanoparticle Interaction: Femto- to Nanosecond Lasers*. Applied Sciences, 2018. **8**(1): p. 112.
88. Hamad, Abubaker Hassan, *Effects of Different Laser Pulse Regimes (Nanosecond, Picosecond and Femtosecond) on the Ablation of Materials for Production of Nanoparticles in Liquid Solution*. High Energy and Short Pulse Lasers, 2014. **23**(9): p. 233-245.